BEATING NYQUIST WITH ULTRAFAST OPTICAL PULSES

by

Bryan T. Bosworth

A dissertation submitted to The Johns Hopkins University in conformity with the requirements for the degree of Doctor of Philosophy.

Baltimore, Maryland

October, 2017

Abstract

Photonic sources readily provide several THz of analog bandwidth for information processing. Taking advantage of this fact, problems such as ultrawideband radio (RF) spectrum sensing, high performance radar, and analog-to-digital conversion can achieve significant performance gains with photonic techniques. Likewise, photonic imaging systems such as time-stretch microscopy have produced a breakthrough in continuous high speed imaging, enabling faster shutter speeds, higher frame rates, and greater gain-bandwidth product than is possible with continuous read-out CCDs and CMOS sensor arrays. However, imaging at this rate with traditional Nyquist sampling inevitably yields sustained data output on the order of 100 Gb/s or more, creating a significant challenge for storage and transmission. Real images and video are highly compressible, so this deluge of data is also highly inefficient.

This thesis will address several techniques based on chirp-processing of ultrafast laser pulses that demonstrate real-time efficient compression of both electronic and optical signals, overcoming electronic bottlenecks via optical processing in the analog domain. Several systems will also be presented that permit greater information ex-

ABSTRACT

traction from high throughput microscopy experiments by measuring quantitative phase images on a time-stretch microscope.

Primary Reader: Mark A. Foster

Secondary Reader: Trac D. Tran

Acknowledgments

I would like to thank my advisor Prof. Mark Foster for his creativity, intelligence, optimism, and willingness to let me try weird things throughout my time working for him. I would like to thank Prof. Trac Tran, Prof. Sang (Peter) Chin, and Dung Tran for our very successful collaboration and for teaching compressed sensing to me. And I would like to thank Prof. Amy Foster and Prof. A. Brinton Cooper for their support on our collaborative projects.

A big "thank you" goes to all of my labmates in the Ultrafast & Nonlinear Photonics Group and the Integrated Photonics Lab for collaborations, useful discussions, help, and patience: Milad Alemohammad, Iskandar Atakhodjaev, Dr. Amit Bhatia, Brian Grubel, Michael Kossey, Kangmei Li, Dr. Keith Petrillo, Jaewook (Jeff) Shin, Jasper Stroud, Hongcheng Sun, and Dr. Hong-Fu Ting.

Lastly, I would love to acknowledge the free software and open-source movements and everyone who takes a chance by freely sharing his or her creative output. The success of my experiments owes a debt to them.

ACKNOWLEDGMENTS

This work was supported by the National Science Foundation (NSF) under Grant EECS-1443936 and the Office of Naval Research (ONR) under Grant N00014-12-1-0730.

Dedication

This thesis is dedicated to my family.

Contents

List of Figures

Chapter 1

Introduction

This thesis is primarily concerned with novel applications of the unique capabilities of ultrafast lasers and optical fiber technologies for high-speed signal acquisition and processing. Several techniques will be introduced for acquisition of electronic and optical signals using chirp processing to achieve optical signal processing for compressed sensing (CS) reconstruction. This introduction describes the relevant background in optics and signal processing for understanding this work. Chapter 2 presents the first demonstration of the chirp processing with CS concept applied to ultrawideband radio frequency (RF) signals. Chapter 3 describes a significant extension of that work to high-resolution acquisition of arbitrary frequencies. Chapter 4 shifts focus to image acquisition with an application of the work to high-speed flow microscopy. Chapter 5 presents a new method for quantitative phase time-stretch microscopy using self-referencing of ultrafast pulses. Finally, chapter 6 describes several

experimental techniques that are still in ongoing development for quantitative phase time-stretch microscopy and chapter 7 offers a few concluding remarks.

1.1 Fiber Optics

In essence, optical fiber extends the theory of electromagnetic waveguides, first conceived at the close of the 19^{th} century [1–3] for radio frequency signals traveling in structures composed of conductors and dielectrics, to light in a cylinder of glass with a microscopic radial refractive index variation. Solutions to Maxwell's equations for the electric and magnetic field that are stable along the length of a structure are known as *modes*. The propagation characteristics of a fiber's fundamental mode such as attenuation at operating wavelengths, dispersion, and nonlinearity are most relevant here.

1.1.1 Fiber Parameters

Optical fibers are principally manufactured from fused silica glass with dopants to produce a small refractive index contrast (e.g., $\Delta = n_{\text{core}} - n_{\text{cladding}} < 0.01$) between the core and cladding. The intersection of Rayleigh scattering and vibrational resonances in silica in the infrared ($\lambda > 7\mu\text{m}$) leads to a relatively wide window in the near-infrared (near-IR) close to 1550 nm with minimum transmission attenuation [4]. The telecommunications C- (1530–1565 nm) and L-bands (1565–1625 nm) are so designated in order to capitalize on the minimum loss possible: Corning SMF-28, for

example, is specified for ∼0.2 dB/km from 1490 nm to 1625 nm. Many other fiber designs naturally exist for special applications (e.g., microstructured and hollow-core fibers for effective refractive indices close to unity and Fluoride fibers for transmission in the mid-IR), but loss and cost are always higher than commodity telecommunications fibers, which will be used throughout this thesis.

1.1.2 Dispersion

In optics, dispersion generally refers to the dependence of refractive index on wavelength (λ), written $n(\lambda)$ or $n(\omega)$ if expressed in terms of optical frequency $\omega = 2\pi\nu$. Critical to all applications with large a bandwidth-distance product (e.g., THz of optical bandwidth and km of fiber) is the phenomenon of temporal broadening as different wavelengths move with different group velocities $v_g = \left(\frac{\partial\beta}{\partial\omega}\right)^{-1}$ where $\beta(\omega)$ is the propagation constant in the medium.

In fiber, dispersion is due not only to the glass properties (material dispersion) but also the waveguiding geometry (waveguide dispersion). Thus, many fiber designs are available that are single-mode (avoiding modal dispersion) yet have very different amounts of normal (red-shifted wavelengths travel faster than blue-shifted) or anomalous (blue-shifted wavelengths travel faster) dispersion.

Dispersion is commonly treated using the spectral phase accumulated through the propagation distance L and the propagation constant $\beta(\omega)$. This is straightforward

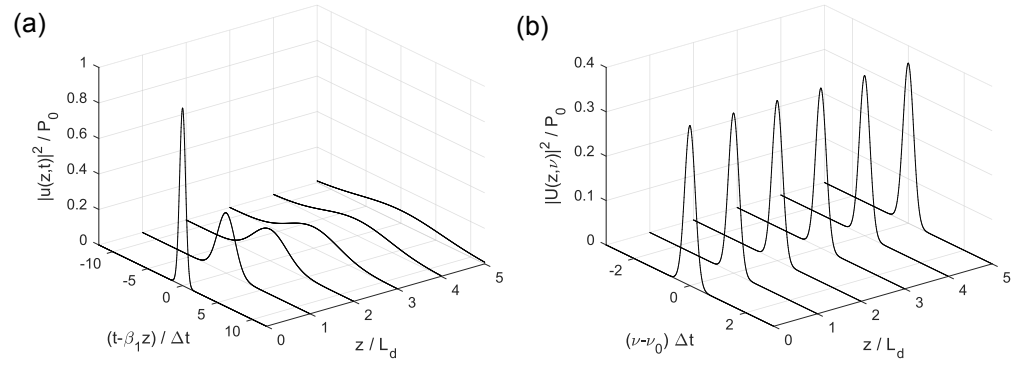

Figure 1.1: Illustration of the temporal (a) and spectral (b) effects of β_2 dispersion without nonlinearity.

to represent with an inverse Fourier transform of the input field $E_{\text{in}}(t) \overset{\text{FT}}{\longleftrightarrow} E_{\text{in}}(\omega)$:

$$E_{\text{out}}(t) = \frac{1}{2\pi} \int E_{\text{in}}(\omega) \exp(-j\beta(\omega)L) \exp(j\omega t)\, d\omega. \tag{1.1}$$

$\beta(\omega)$ is commonly represented by a Taylor expansion around the center frequency of the laser ω_0: $\beta(\omega) = \beta(\omega_0) + \beta_1(\omega - \omega_0) + \frac{1}{2}\beta_2(\omega - \omega_0)^2 + \frac{1}{6}\beta_3(\omega - \omega_0)^3 + \ldots$ where $\beta_n = \partial^n\beta/\partial\omega^n$. The terms represent the phase velocity $v_p = \omega_0/\beta_0$, group velocity v_g (see above), group velocity dispersion (GVD or second-order dispersion), third-order dispersion (TOD), and so on.

Figure 1.1 depicts the effect of GVD (β_2) on a Gaussian optical pulse with a power full-width at half-maximum of Δt (adapted from [5, 6]). The time window is moving with the pulse at its group velocity (in normalized retarded time $\tau = (t - \beta_1 z)/\Delta t$) and depicted at propagation distances that are multiples of the dispersion length defined $L_D = \Delta t^2/|\beta_2|$. L_D provides a characteristic length scale over which the duration

of a pulse will change noticeably due to GVD (Fig. 1.1(a)). Because the effect is contained in the spectral phase, the spectral power in Fig. 1.1(b) remains unchanged. For propagation through many dispersion lengths, it is also convenient to express pulse duration using the pulse spectral width $\Delta\lambda$ and the parameter $D = -2\pi c\beta_2/\lambda^2$ (generally in units of ps/nm-km): $\Delta t = D\Delta\lambda L$ [7].

1.1.3 Nonlinearity

Optical nonlinearity concerns the dependence of material refractive index on the field traveling in the medium. In this domain, the well-known scalar polarization density of the medium $P = \epsilon_0\chi_e E$ (ϵ_0 is the permittivity of free space and χ_e is the electric susceptibility), which is linear with the electric field E, must be supplemented with additional terms

$$P = \epsilon_0 \left[\chi^{(1)}E + \chi^{(2)}E^2 + \chi^{(3)}E^3 + \ldots\right] \tag{1.2}$$

where χ^n is the n^{th} order susceptibility. We ignore χ^2 because it is nonzero only in crystals that lack inversion symmetry; therefore, it is absent in glass. χ^3, however, is present in all materials and the E^3 term gives rise to a nonlinear refractive index $n_{\text{NL}} = n(\omega) + n_2|E|^2$ where n_2 is the nonlinear coefficient of the material (proportional to $\chi^{(3)}$) in units of inverse irradiance [m^2/W].

Nonlinearity in optical fiber is a very rich topic that covers a plethora of interesting phenomena [5]. For the purpose of this discussion, it is important to mention that all solid-core single-mode fibers have a noticeable nonlinearity conveniently summarized by the nonlinear coefficient

$$\gamma = \frac{2\pi n_2}{\lambda_0 A_{\text{eff}}} \tag{1.3}$$

where the nonlinear coefficient n_2 is assumed to be spatially uniform and A_{eff} is the effective fiber mode area $A_{\text{eff}} = \frac{\left(\iint |u(x,y)|^2 \, dx \, dy\right)^2}{\iint |u(x,y)|^4 \, dx \, dy}$ [m^2] for the electric field spatial profile $u(x, y)$ with λ_0 center wavelength. A typical single-mode fiber for $\lambda_0 = 1550$ nm, for example, has the parameters $A_{\text{eff}} = 80$ μm^2, and $n_2 = 2.7 \times 10^{-20}$ m^2/W, yielding $\gamma = 1.37$ (W-km)$^{-1}$. Special fibers with higher confinement (smaller A_{eff}) at shorter wavelengths can have γ values 1–2 orders of magnitude higher.

Together with the propagation constant $\beta(\omega)$ (see section 1.1.2), γ can be used to describe the propagation of short pulses via the nonlinear Schrödinger equation (NLSE), which has the form [7]

$$\frac{\partial u}{\partial z} - \frac{j\beta_2}{2}\frac{\partial^2 u}{\partial t^2} + j\gamma|u|^2 u = 0, \tag{1.4}$$

ignoring higher order dispersion and other nonlinearities such as Raman scattering.

Nonlinear pulse shaping (see also section 1.2.2) is a constant fixture in this work before the encoding stages and the effects of self-phase modulation

must always be considered when trying to maintain the spectrally-encoded information of the succeeding chapters.

1.1.4 Devices

The success of fiber optic communications has led to a wide array of relatively affordable fiber-coupled modulators for optical intensity, phase, and IQ modulation, fiber-coupled high-speed detectors, and serial pattern generators for wavelengths near 1550 nm. High-frequency modulators (10–35 GHz and above) are based on lithium niobate ($LiNbO_3$), which provides large electro-optic coefficient, low attenuation, and low chirp. Waveguides are formed by indiffusion of titanium to form the core and RF electrodes are fabricated on top of the crystal to drive the electro-optic refractive index modulation [8]. Phase modulators can be manufactured from a straight waveguide with electrodes. Intensity and IQ modulators employ one or more waveguide Mach-Zehnder interferometers with additional biasing electrodes to select the operating region of the optical power vs. input voltage transfer function.

These components as well as standard single-mode fiber, dispersion-shifted fibers, and fiber mode-locked lasers (see section 1.2) are crucial to all of the work presented in this thesis.

1.1.5 Amplification

Erbium-doped fiber amplifiers (EDFAs) produced more than an order of magnitude improvement in the capacity (i.e., bandwidth-transmission distance product) of fiber communication systems after their invention in the 1980s [4, 9]. The combination of high small-signal gain (>30 dB), low minimum input power, low noise figure (close to the theoretical limit of 3 dB), and broad gain bandwidth (10s of nm near 1550 nm) make EDFAs key components in high-capacity wavelength division multiplexed photonic communication links.

As will become apparent in chapters 4–6, they also provide an excellent inline optical preamplifier for detecting high-speed image frames encoded on ultrafast laser pulses. Light amplification (as opposed to electronic gain after detection) within the flow of information for an imaging system is generally possible only with fiber-based imaging systems and EDFAs provide the most robust and widely available optical amplifier.

1.2 Ultrafast Optics

Ultrafast optics describes the science and applications of pulsed lasers capable of generating ultrashort light pulses. Such pulses are bursts of light with durations on the order of 1–100 femtoseconds (fs, defined as 10^{-15} seconds), though new subfields have opened up concerned with extremely short attosecond (as, defined as 10^{-18}

seconds) phenomena. Such short durations imply exceptional temporal and spatial (100 fs $\times$ 3×10^8 m/s = 30 μm) resolution, broad bandwidth (determined by Fourier relationship) easily extending over several THz, as well as the potential for high peak powers of kW or more at typical repetition periods even at modest average optical power (i.e., well below 1 W). This makes ultrafast sources essential to numerous applications such as time-resolved spectroscopy, frequency metrology, laser cutting and additive manufacturing, and biomedical imaging [7].

1.2.1 Sources

The most common ultrafast lasers are so-called mode-locked lasers, which resemble conventional lasers except that they are designed for broadband operation with up to many thousands of longitudinal modes oscillating simultaneously. Unlike a conventional multi-mode laser, all mode-locked lasers include an intra-cavity loss mechanism that will cause the laser to favor pulsed operation rather .than free-running continuous wave (CW) operation. That is, when mode-locked a laser supports propagation of an optical pulse that if observed at given location appears steady with each round trip through the laser cavity. The exact pulses that a specific laser can generate involve a complex interplay between the laser medium's gain characteristics, the intra-cavity dispersion and nonlinearity, attenuation, and the temporal and spectral effects of the mode-locking mechanism. Thus, there is a wide variety of mode-locked laser designs with different gain media, dispersion management,

and mode-locking schemes. Correspondingly, for any center wavelength (determined by the gain medium) desired there is frequently a cluster of possible pulse widths, energies, and temporal and spectral profiles.

This intra-cavity loss mechanism can be either active or passive. Active mode-locking almost always implies the use of an intensity modulator inside the cavity, externally-driven by an RF source at a multiple of the natural cavity repetition frequency $f_{rep} = 1/\tau_{\text{rep}}$ where τ_{rep} is the cavity round-trip time. Either the RF source can be tuned to (or derived from) the cavity length or (more commonly) the cavity length can be adjusted to the source. Actively mode-locked lasers are capable of very high-repetition rates (e.g., 10–20 GHz) in the case of harmonic mode-locking and straightforward synchronization with other electronics; however, pulse durations are generally limited to 1 ps and longer. Passive mode-locking achieves the shortest pulses at the expense of repetition rate and ease of synchronization. It is achieved without external driving through the use of a saturable absorber that exhibits lower loss at high optical fluence than low fluence. Either a slow saturable absorber such as a semiconductor saturable absorber mirror (SESAM) or fast absorber such as the nonlinear refractive index as a means for polarization rotation or spatial self-focusing can be used.

1.2.2 Ultrafast Pulse Shaping

Pulse shaping refers to the use of active (in the case of electro-optics) or passive optical methods to alter the temporal or spectral profile of the optical pulses

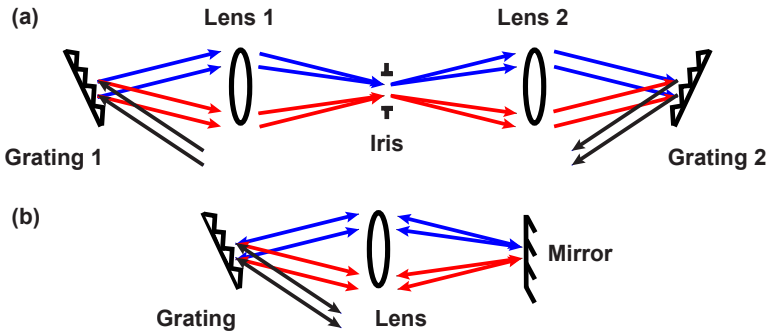

Figure 1.2: 4-f pulse shaper designs with (a) two gratings and lenses for better manipulation of the optical spectrum (imaged to a line at the iris) or (b) one grating and one lens for compactness and simplicity of alignment.

in a system. Creation of pulse stacks, dispersion management, amplification, and customization of pulse profile are just a few of its applications [10–15].

One of the canonical means for ultrafast pulse shaping is the 4-f pulse shaper (Fig. 1.2). A diffraction grating and spherical lens at one focal length (f) separation form a line image of the source's optical spectrum at a distance f after the lens (i.e., utilizing the Fourier transform property of lenses [16]). The spectrum at this plane can be modified either by a simple aperture (acting as a bandpass filter), a printed transparency mask, or a phase or amplitude modulator such as a liquid crystal spatial light modulator (SLM) [12, 17]. To recombine the filtered line into a high quality beam, either a mirror can be placed at the image plane and the light reflected through the same lens and grating or a second lens and grating can be added. The mirror affords compactness and simplicity of alignment; the dual lens and grating approach simplifies exact placement of the mask at the image.

The basic 4-f pulse shaper with no mask or filter can also be freely reconfigured using different magnification telescopes [18] (the basic configuration described above forms a $1\times$ magnification telescope with the lens and mirror or pair of lenses) and distances between the lenses and gratings to create temporal stretching or compression.

Several of the innovations presented in this thesis can be considered pulse-shaping techniques; the 4-f pulse shaper will also reappear in multiple novel configurations.

1.2.3 Chirp Processing

Optical pulses which are as temporally short as their bandwidth permits are known as *transform-limited*. However, as shown in section 1.1.2, spectral phase on the orders of β_2 and above causes the optical frequency content to be distributed in time away from the pulse center frequency, which is known as *chirp*. β_2 contributes linear chirp or a linear mapping of frequency versus time. This is easily seen in the spectrograms of Fig. 1.3 computed from the pulse at $z = 0$ and $z = 5L_D$ in Fig. 1.1: for the input pulse (a) all of the frequency content is at time zero, but for the dispersed pulse (b) the frequency content is linearly distributed in time . Higher order dispersion causes other nonlinear frequency mappings that are important and ever-present, but beyond this discussion.

The management of chirp through choice of fiber parameters or, in free-space, through pulse shapers or diffractive stretchers/compressors is essential to high peak power pulse delivery for, e.g., nonlinear microscopy and dozens of other applica-

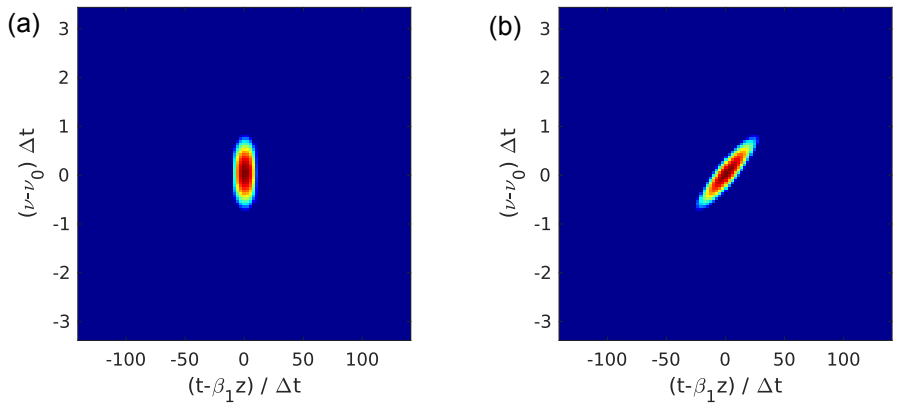

Figure 1.3: Spectrograms computed at (a) $z = 0$ and (b) $z = 5L_D$ from the propagation example in Fig. 1.1. Colormap is computed from power on logarithmic scale.

tions. The possibility of temporally stretching and compressing a pulse in a matched way is essential to high performance amplification, known as chirped pulse amplification (CPA) [19], where high peak powers would otherwise cause too much nonlinearity or damage the optical system.

A particularly rich application of chirp processing relies on the time-space duality of pulse propagation and spatial diffraction [20, 21]. In the absence of nonlinearity ($\gamma = 0$), Eq. (1.4) simplifies to

$$\frac{\partial u}{\partial z} = \frac{j\beta_2}{2}\frac{\partial^2 u}{\partial t^2}, \tag{1.5}$$

which directly resembles the equation for paraxial diffraction of a monochromatic wave

$$\frac{\partial u}{\partial z} = \frac{-j}{2k}\left(\frac{\partial^2 u}{\partial x^2} + \frac{\partial^2 u}{\partial y^2}\right) \tag{1.6}$$

with β_2 equivalent to $-k^{-1}$ and t equivalent to x or y. For $\beta_2 z \to 0$, the pulse exists in the so-called near-field regime analogous to Fresnel diffraction. For $z \gg L_D$ or $|\beta_2 z| \gg T^2/8$ where T is the full duration of the input pulse, the pulse exists in the far-field regime analogous to Fraunhofer diffraction [7,16]. Another useful property of diffraction appears here because the far-field version of the electric field is the Fourier transform of the input field, but the transform yields the optical spectrum rather than spatial frequency content. In another sense, the spectrogram of the dispersed pulse (Fig. 1.3(b)) tilts so far that the temporal profile of the pulse directly reflects the optical spectrum with the mapping constant $\frac{\partial w}{\partial t} = \frac{1}{\beta_2 z}$. Unlike diffraction, β_2 and D can be designed to take both signs so the temporal transformation can be easily reversed.

The ability to create a custom mapping of optical spectrum into time creates several interesting possibilities. Optical spectra customized with a pulse shaper can be serve as arbitrary temporal waveforms at extremely short timescales [13, 14]. Conversely, high-speed phenomena that can be imprinted onto a pulse can be used to shape the optical spectrum for read out using a simple optical spectrum analyzer [10, 11, 15]: repetitive events that can be synchronized to the laser can be read out with higher sensitivity scanning spectrometers, but nonrepetitive events require a parallel spectrometer (i.e., a non-scanning sensor array) and higher pulse energies. This issue will be discussed further in chapter 2.

1.3 Compressed Sensing

Compressed sensing, also known as compressive sensing, is a new subfield of mathematics and signal processing and representation that has received considerable interest during the past decade since its introduction by Candès, Tao, Romberg, and Donoho in 2006 [22–26]. The core insight of CS is that the natural sparsity of real signals when represented in an appropriate mathematical basis can be utilized to permit accurate reconstruction from a small number of measurements far fewer than the Nyquist dimension of the signal. Rather than sample at a rate greater than or equal to twice the signal bandwidth, adhering to the Nyquist theorem, CS advocates the acquisition of a small number of inner-products between the signal of interest and known patterns with feature sizes fine enough to represent the signal bandwidth.

By reducing the number of necessary measurements, hardware designed for CS can operate more efficiently using less power, data transmission, and storage [27, 28]. Important for this work, CS can also alleviate traditional bottlenecks where high-rate electronic sampling is impossible or limited in throughput [29].

1.3.1 Traditional Compression

Compression of image, audio, and video signals underpins the modern digital world of streaming media and endless user-generated content. After digitization with a pixel array or transducer and ADC, the full Nyquist version (with the inherent reso-

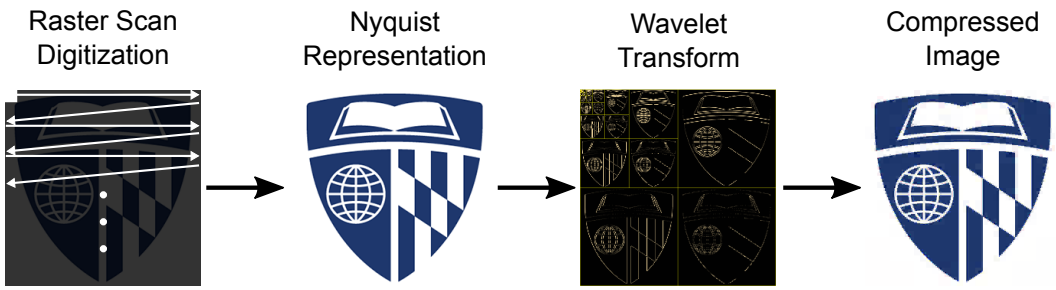

Figure 1.4: Example of traditional image compression wherein only 5% of the coefficients in an 8-level Haar wavelet transform are kept to reconstruct the image.

lution of the sensor) exists briefly in device memory before undergoing a compression routine that will try to discard as much information as possible without losing perceptual quality. Commonly, this involves a process of sparse approximation wherein the signal is transformed to a basis such as a local discrete cosine transform (DCT, used in JPEG) or multi-level wavelet transform (used in JPEG 2000). The goal is to achieve a complete (i.e., invertible) representation of the signal that confines its energy to a small number of significant coefficients so that the rest of the coefficients can be thresholded and discarded. Thresholding implies lossy compression, incapable of recovering a bit-accurate version of the original, but small approximation error with high compression ratios (>10:1) are readily achieved. An example appears in Fig. 1.4 where the JHU shield is acquired with a raster scan and compressed using an 8-level Haar wavelet transform, keeping only 5% of the original entries according to significance: the sparsity in the wavelet domain is immediately apparent and the loss of perceptual quality is very acceptable.

1.3.2 CS Acquisition

CS measurement is conventionally represented as a matrix multiplication

$$\boldsymbol{y} = \boldsymbol{\Phi x} \quad \text{where} \quad \boldsymbol{\Phi} = \begin{bmatrix} -\boldsymbol{\phi}_1 - \\ -\boldsymbol{\phi}_2 - \\ \vdots \end{bmatrix}. \tag{1.7}$$

$\boldsymbol{x}$ is the signal of interest with its full Nyquist dimension N and $\boldsymbol{\phi}_k$ are the known measurement functions (also dimension N). In the case of a Nyquist measurement with a shifted Kronecker delta function (i.e., raster scan or conventional parallel 2D imaging array) or a basis scan with, e.g., a series of tones at different frequencies as in a spectrum analyzer, $\boldsymbol{\Phi}$ will have dimensions $N \times N$. However, because a sub-Nyquist representation is desired, $\boldsymbol{y}$ is smaller than $\boldsymbol{x}$ and $\boldsymbol{\Phi}$ is often called a "short and fat" matrix with dimensions $M \times N$ where $M < N$ (see Fig. 1.5). This is an inverse problem that gives rise to infinitely many solutions $\hat{\boldsymbol{x}}$ since $\boldsymbol{\Phi}$ has a null space. Thus, it is necessary to put conditions on $\boldsymbol{\Phi}$ and $\boldsymbol{x}$ to guarantee accurate recovery of $\boldsymbol{x}$.

The solution is sparsity. Most often, $\boldsymbol{x}$ is a dense signal with many non-zero values but there is often a basis or dictionary such as frequency or wavelet in which $\boldsymbol{x}$ is sparse with very few significant coefficients. $\boldsymbol{x}$ can thus be represented $\boldsymbol{x} = \boldsymbol{\Psi}^{-1}\boldsymbol{s}$ where $\boldsymbol{\Psi}$ is the forward transform to the sparse basis. The sensing operation is now $\boldsymbol{y} = \boldsymbol{A}\boldsymbol{s}$ where $\boldsymbol{A} = \boldsymbol{\Phi}\boldsymbol{\Psi}^{-1}$. It can then be shown that for $\boldsymbol{A}$ matrices with low coherence, defined as the maximum inner product between any two normalized columns

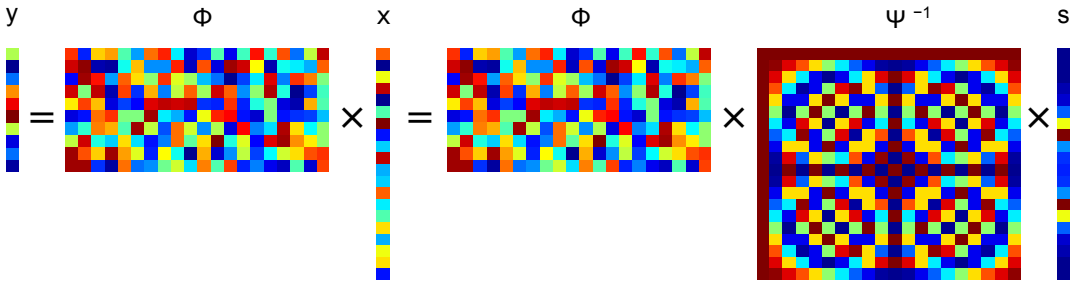

Figure 1.5: Illustration of CS with output vector $\boldsymbol{y}$, signal $\boldsymbol{x}$, random measurement matrix $\boldsymbol{\Phi}$, sparsifying DFT transform $\boldsymbol{\Psi}$, and sparse vector $\boldsymbol{s}$.

(denoted $\boldsymbol{a}_i$ and $\boldsymbol{a}_j$) $\mu(\boldsymbol{A}) = \max_{i \neq j} |\langle \boldsymbol{a}_i, \boldsymbol{a}_j \rangle|$, sufficiently sparse $\boldsymbol{s}$ can be recovered exactly. That is, $\boldsymbol{A}$ satisfies the Restricted Isometry Property

$$(1 - \delta_{2S}) \|\boldsymbol{s}\|_2^2 \leq \|\boldsymbol{A}\boldsymbol{s}\|_2^2 \leq (1 + \delta_{2S}) \|\boldsymbol{s}\|_2^2 \tag{1.8}$$

for all S-sparse (i.e., containing S nonzero entries) vectors $\boldsymbol{s}$ with a small constant $\delta_{2S} < \sqrt{2} - 1$. Thus, $\boldsymbol{A}$, the product of the sampling matrix and sparsifying transform, approximately preserves the length of S-sparse vectors, implying that such sparse vectors cannot be in the null space of $\boldsymbol{A}$. This guarantees that the S-sparse vectors can be recovered exactly via ℓ_1 minimization

$$\min_{\hat{\boldsymbol{x}} \in \mathbb{R}^n} \|\hat{\boldsymbol{x}}\|_1 \quad \text{subject to} \quad \boldsymbol{y} = \boldsymbol{A}\hat{\boldsymbol{x}} \tag{1.9}$$

and approximately S-sparse vectors can be recovered almost as well as if the S most significant coefficients were measured directly [30].

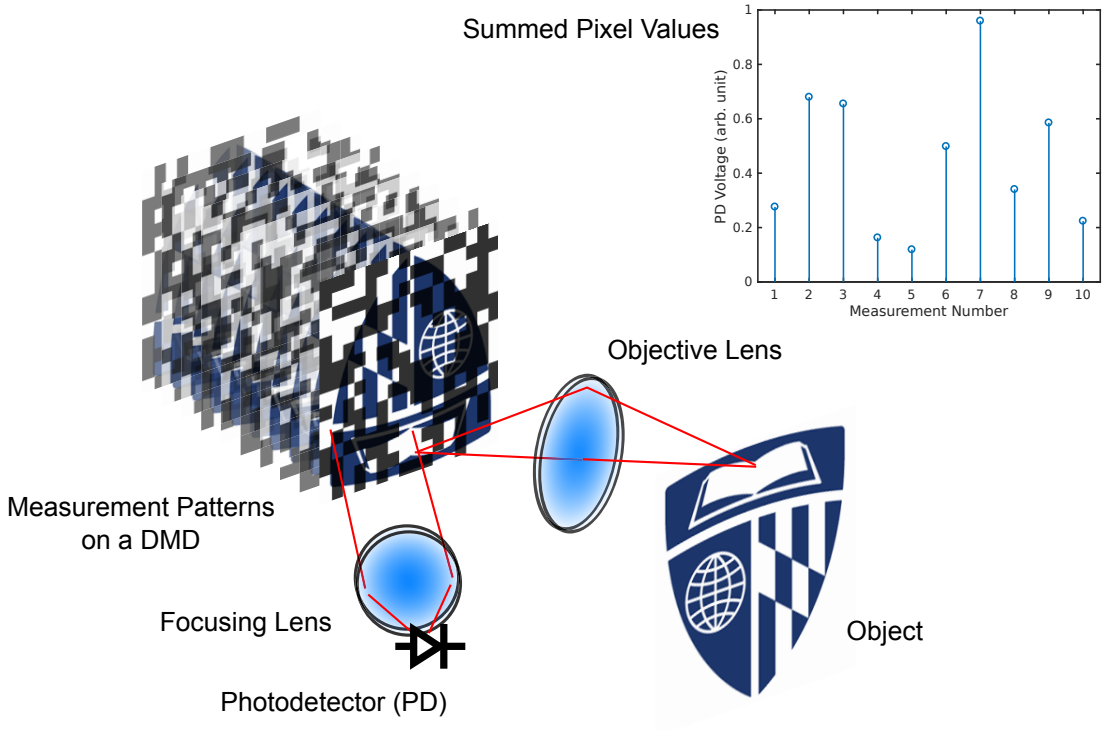

Figure 1.6: Schematic diagram of CS single-pixel camera acquisition.

The most well-known CS architecture for image signals is the single-pixel camera (Fig. 1.6) [31]. In this camera, the conventional pixel array sensor is traded for a digital micromirror device (DMD) and focusing lens onto a photodetector and ADC. A highly sub-Nyquist number of random patterns are displayed in succession on the DMD and the summed optical power is recorded for each, effectively computing the inner product in Eq. (1.7) in the optical domain. Because approximately half of the pixels are turned on per pattern, a full image can be formed with better SNR than a raster scan in less time than a full basis scan [32]. This architecture will be discussed further in section 4.4.

Chapter 2

Stationary RF Sensing

In this chapter, we introduce spectral encoding of highly-chirped ultrafast laser pulses with pseudorandom bit sequences such that every laser pulse acquires a unique spectral pattern. The pulses are partially compressed in time, extending the effective sampling rate beyond the electronic limit, and then modulated with a sparse microwave signal. Finally the pulses are fully compressed and detected, effectively integrating the measurement. We achieve 100 usable features per pattern allowing for 100 points in the reconstructed microwave spectra and experimentally demonstrate reconstruction of 2-tone and 3-tone microwave signals spanning from 900 MHz to 14.76 GHz. These spectra are reconstructed by measuring the energy of only 23 to 38 consecutive laser pulses acquired in a single-shot with a 500-MHz real-time oscilloscope.

2.1 Radio Spectrum Sensing

In consumer and military wireless communications, it is often desirable to detect and manage radio frequency (RF) spectrum usage rapidly across multiple frequency bands. Though the radio spectrum is already tightly allocated, actual usage at any single time tends to be very sparse [33] with a limited number of channels in use, scattered across an extremely broad bandwidth.

One straightforward approach to fast RF frequency analysis is to sample in the temporal domain at the Nyquist rate and apply a Fast Fourier Transform, but measuring signals with a bandwidth of 20–30 GHz or more is challenging for electronic analog-to-digital converters (ADCs). For this reason, photonic systems, which offer very large instantaneous bandwidth are an attractive solution for microwave signal processing.

Recently, several applications of CS and microwave photonics to RF frequency detection were demonstrated experimentally. In [34], the random demodulation technique proposed in [35] was implemented optically with a continuous wave (CW) laser and two Mach-Zehnder modulators (MZMs) for RF and PRBS modulation in succession; a single tone near 1 GHz was successfully reconstructed. In [36], frequency recognition and downconversion of two tones were demonstrated inside a 5 GHz bandwidth between 15 and 20 GHz using a PRBS MZM and an RF MZM with two outputs and a balanced detector. In [37], a mode-locked laser (MLL) with an RF MZM following a significant amount of fiber dispersion was used with a 118-pixel spatial light modulator (SLM) in a 4-f pulse shaper to accomplish pseudorandom bit sequence

(PRBS) modulation of a wavelength-to-time-to-1D spatial mapping. Two microwave tones at 71.42 and 214.16 MHz were successfully reconstructed.

Several other systems have also been proposed in simulations [38–40]. Of interest here, the possibility of dispersing MLL pulses in optical fiber, modulating with an RF test signal, and dispersing them further with a second fiber for a desired amount of temporal magnification [41] was proposed in [40]. However, this approach called for PRBS mixing electronically after photodetection, limiting its use of optical information processing. The detection of long-time dispersed pulses would also enforce low peak-to-average power at the photodetector (PD) and long electronic integration times limiting the measurement speed and signal-to-noise ratio (SNR).

2.2 Experimental System

In the system presented here (Fig. 2.1), ultrafast MLL pulses are chirped to spread the optical spectrum over several ns in time. They are then modulated to encode a different known PRBS pattern on each consecutive pulse's spectrum. The PRBS patterns form the set of ϕ_k's with N random spectral features encoded on the kth pulse. After PRBS modulation, the pulses are partially compressed in time, which increases the feature rate and thereby the maximum recoverable RF frequency. These partially compressed pulses are modulated once more with the sparse-frequency RF signal under test (x), which yields the mixed PRBS patterns $\times$ RF signal encoded

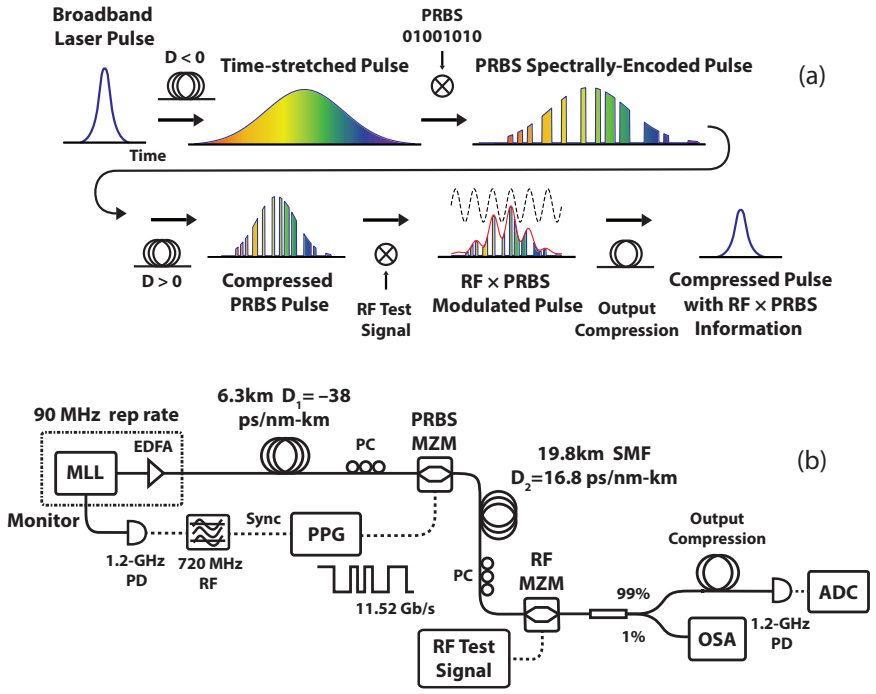

Figure 2.1: (a) Conceptual operation. (b) Detailed experimental system.

on their spectra. Finally, each optical pulse is fully compressed bringing the full spectral content to one point in time prior to the PD. The second mixing stage and full pulse compression respectively perform the inner product between the PRBS and RF signals by first piecewise multiplying the PRBS and RF signal and then summing the products. The compressed pulse acts as an impulse to the relatively slow detector, which therefore measures the pulse energy and allows one digital sample to carry the full RF×PRBS inner product. By performing this summation optically we facilitate high SNR photodetection and enable single-shot digitization of the measurements (y_k) with an ADC much slower than the effective sampling rate of the system. Thereby, the CS measurements y_k are rapidly acquired at the pulse

repetition rate of the MLL. These measurements y_k are fed into a minimization algorithm, described later, to recover the RF signal x.

Similar to [37], we employ chirping-based optical-wavelength-to-time mapping for information processing, however we acquire unique pseudorandom measurements at the laser repetition rate (90 MHz) rather than the SLM refresh rate ($\sim$100 Hz), a 5–6 orders of magnitude improvement in measurement speed. Furthermore, by applying the PRBS modulation entirely with fiber-based components, we reduce optical losses and alignment sensitivity inside the system, also aiding output detection. Use of a 2D SLM and parallel high-speed PDs and ADCs was proposed in [6] to permit fast, concurrent pseudorandom measurements of RF signals, unaffected by the SLM refresh rate. However, this approach requires splitting the laser pulse amongst M parallel detection circuits leading to greater hardware complexity.

The specific experimental system consists of an erbium fiber MLL emitting pulses at $f_{\text{rep}} = 90$ MHz ($\tau_{\text{FWHM}} = 300$ fs). These pulses are spectrally broadened and sent into a normal dispersion fiber for optical wavelength-to-time mapping. An erbium-doped fiber amplifier (EDFA) immediately following the oscillator inside the MLL provides some spectral broadening through self-phase modulation (SPM) in addition to high peak power at the system input. This combines with the high dispersion ($D_1 = -38$ ps/nm-km) and modest nonlinearity ($\gamma = 3.8$ W^{-1}km^{-1}) of the 6.3-km-long normal dispersion fiber to yield pulses that span greater than 30 nm in spectral bandwidth at -6 to -7 dB and 8.5 ns in time.

These chirped pulses are sent into an electro-optic Mach-Zehnder intensity modulator (MZM) driven by a pulse pattern generator (PPG) for random temporal modulation which in turn imposes the random pattern onto the spectrum of the highly chirped pulses. The PPG outputs digital 1s and 0s at a rate of 11.52 Gbit/s or 128 bits per laser pulse period. Here, the chirped pulses span less than the full period and the pattern length is set to $N = 100$. The PPG modulates the optical field at the PRBS MZM with user-programmable patterns up to 1.3 Mbit in length; customized patterns are used, allowing for more than 10,000 unique pseudorandom signals (although we typically use <40). Each optical pulse serves as a single pseudorandom measurement of the RF test signal, and the analog-to-digital conversion of the pulse energies is performed in a single-shot without averaging, such that measurements are obtained at the 90 MHz repetition rate and a full set of $M < N$ measurements can be acquired in only a few hundred ns.

Figure 2.2 illustrates the density of PRBS features that are modulated onto the pulse spectra, depicting 0101... and 1010... in Fig. 2.2(a) and one example pseudorandom modulation pattern as well as the spectral envelope for reference in Fig. 2.2(b). These patterns are detected on an optical spectrum analyzer (OSA) at the system output without an RF test signal and represent the temporal pattern due to the wavelength-to-time mapping of the highly chirped pulses. The full dimension N of the signal to be reconstructed is determined by the spectral width ($\Delta\lambda$) above a user-defined threshold after nonlinear broadening,

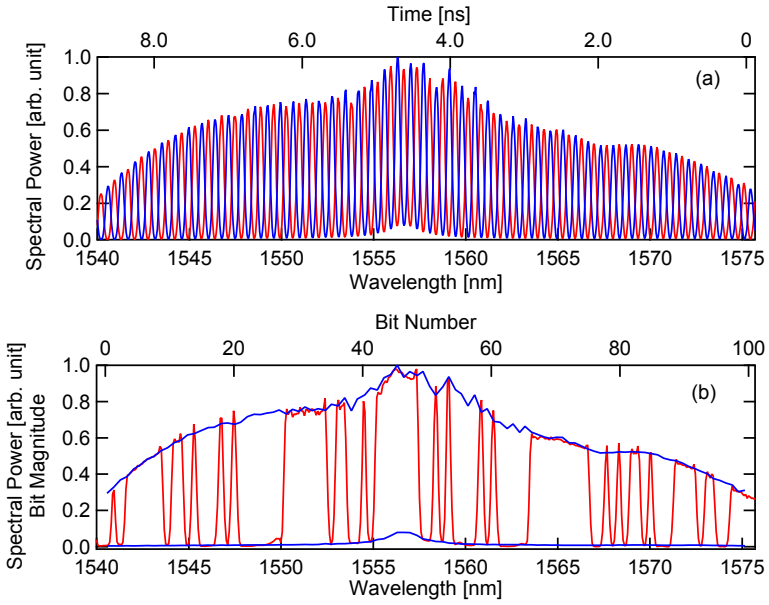

Figure 2.2: Example optical spectra showing (a) 0101... (blue curve) and 1010... (red curve) pattern modulation and (b) an example PRBS pattern (red curve) plotted with the high and low envelopes (blue curves) for pattern modulation used by the reconstruction matrix A in Eq. 2.4.

the dispersion (D_1) and length (L_1) of the time-stretching fiber, and the PPG pseudorandom modulation rate (R_{PRBS}) such that

$$N \approx D_1 L_1 \, \Delta\lambda \, R_{\mathrm{PRBS}}. \tag{2.1}$$

The current results utilize spectral thresholds of -6 to -7 dB to achieve $N = 100$ (Fig. 2.2), yielding a resolution bandwidth RBW $= f_{\max}/(N-1) = 150$ MHz, where $f_{\max}$ is the upper limit for frequency reconstruction (14.9 GHz here). An optical band-pass filter is not employed to remove the spectral content below the spectral threshold. Experimentally, we found this has negligible impact on signal recovery performance. The dispersion, length, and spectral width are easily tunable by choice of fiber and

operating conditions of the MLL. Higher-rate PRBS signal generators are also widely available. Furthermore, the measurement rate of the system is highly customizable by selection of the MLL or by temporal multiplexing of the laser pulse train.

After pseudorandom modulation, the pulses are compressed in time using a 19.8-km-long anomalous dispersion fiber ($D_2 = 16.8$ ps/nm-km) by a factor of 2.58. This increases the effective sampling rate provided by the pseudorandom modulation to 29.8 GS/s. In this way, we set the upper limit for frequency reconstruction of this system at $f_{\max} = 14.9$ GHz to complement the limitations of the RF MZM. Importantly, the length of the compression fiber is easily reconfigured to increase the RF frequency bandwidth of the system. Due to the available spooled fiber lengths, the anomalous dispersion fiber used here overcompensates the dispersion of the stretching fiber, and the PRBS patterns at the output are time-reversed. The PRBS compression causes gaps between measurement pulses. This is not a concern for sparse-frequency signals, which are inherently long-lived in time. Elimination of this gap is possible with a small reduction in the sampling randomness by chirping beyond the repetition period before PRBS modulation and compressing to the full period before RF modulation.

Subsequently, the pulses pass through a second MZM for modulation with an RF test signal. The system is designed for binary PRBS and linear RF modulation. The PRBS modulation depth is greater than 15 dB across nearly the whole usable spectrum, and the spectrum-to-time mapping makes it simple to use the optical spectrum analyzer (OSA) to characterize the full modulation function $R(t)$ such that

after the output of the RF MZM, the optical power is

$$P(t) = R(t)[1 + \alpha x(t)], \tag{2.2}$$

where α is the modulation depth of the RF MZM (approximately 0.5 here). Each measurement y_k is then given by the integral of this intensity with the integral of the random modulation alone subtracted

$$y_k = \int_{-t_r/2}^{t_r/2} R(t)[1 + \alpha x(t)]\,\mathrm{d}t - \int_{-t_r/2}^{t_r/2} R(t)\,\mathrm{d}t, \tag{2.3}$$

where t is a time frame centered on pulse k and t_r is the pulse repetition period. Optical compression of each measurement pulse with 2.5 km of normal dispersion fiber achieves this integration in the optical domain prior to the ADC. Finally, the pulses are measured using a 1-GHz photodiode and digitized in a single-shot using a 500-MHz real time oscilloscope.

2.3 Reconstruction Algorithm

Compressed sensing is motivated by the fact that many signals of interest x have a sparse representation s in an appropriate orthonormal basis Ψ: $s = \Psi x$ and $x = \Psi^{-1}s$. For this system, which seeks a sparse frequency signal, Ψ is a matrix representing the Discrete Fourier Transform (DFT). Thus, the

sparse signal measurement can be represented as

$$y = As + n, \tag{2.4}$$

where $A = \Phi\Psi^{-1}$ and n is additional noise. We use the Gradient Projection for Sparse Reconstruction (GPSR) algorithm [42] to solve the minimization problem

$$\min_s \left(\frac{1}{2}\|y - As\|_2^2 + \tau\|s\|_1 \right), \tag{2.5}$$

where $\|y - As\|_2^2$ is the sum squared error between the measurement vector y and a candidate reconstruction s, $\|s\|_1$ is the ℓ_1 norm of the candidate reconstruction, and the coefficient $\tau > 0$ is a small sparsity-promoting constant that pushes small components of s to zero.

2.4 Experimental Results

To illustrate the encoding of a multi-tone RF signal onto the optical spectrum, Fig. 2.3(a) depicts the difference spectrum between the RF modulated and unmodulated states without PRBS modulation as well as the shape of the optical spectrum alone overlaid for reference. Figure 2.3(b), shows the difference signal with the spectral envelope removed as well as an experimental temporal RF reconstruction from compressed sensing measurements overlaid, showing excellent agreement.

Our results (Fig. 2.3(b–e)) demonstrate accurate reconstruction of the spectral and temporal representations of sparse-frequency RF signals composed of several tones at high multiples of the laser repetition rate. RF tones at non-harmonics of the repetition rate result in a deterministic phase-slip for each tone at frequency f_{RF} of $\Delta\phi = 2\pi f_{\mathrm{RF}}/f_{\mathrm{rep}}$ between measurement pulses. This effect can be addressed in the reconstruction, e.g. by building it into the sparse basis Ψ, and such an implementation will be the subject of future work. Sinusoids at 900 MHz, 2.43, 4.95, 9.9 GHz, and 14.76 GHz were successfully reconstructed in different groups of two or three tones with varied input powers. The two- and three-tone signals were reconstructed into $N = 100$ frequency bins across 14.9 GHz of bandwidth with $M = 23$ and $M = 28$ measurements for two tones (Fig. 2.3(c) and Fig. 2.3(d), respectively) and $M = 38$ measurements for three tones (Fig. 2.3(e)). The reported value of M was chosen to correspond to the first local minimum of the amplitude mean squared error (MSE) reached while increasing the number of measurements M used for reconstruction [37]. The experimental compression ratios (M/N) were thus 23–38% depending on the signal complexity. Measurements were acquired in a single-shot, such that the measurements for a full two-tone reconstruction, e.g. Fig. 2.3(d), were captured in $\sim$250 ns given the 90-MHz MLL repetition rate. Test signals were spaced throughout the 14.9 GHz bandwidth without affecting the number of necessary measurements, demonstrating the large instantaneous bandwidth of the system. This is particularly evident in Fig. 2.3(e) where a test signal with

wide spanning frequency content of 900 MHz, 4.95 GHz and 14.76 GHz and 10-dB variation in amplitude are faithfully reconstructed.

Compressed sensing theory predicts that pseudorandom sampling with a symmetric Bernoulli distribution (our PRBS) permits accurate recovery of a sparse signal with S non-zero components with excellent probability for $M \geq C \cdot S \log(N/S)$ where C is a small constant that depends on the test case [30]. Using 38 measurements for three tones and 23–28 for two tones demonstrates this approximately linear scaling in M for small S.

Notably, this system achieves reconstruction of signals up to 14.9 GHz using a 500-MHz digitization bandwidth. Thus, the demonstrated PRBS modulation and photonic time-stretching/compression technique reduces the required ADC bandwidth by a factor of >30. Moreover, by adjustment of the partial-compression fiber length, the detection bandwidth can be extended far beyond 14.9 GHz, limited primarily by the RF MZM. Also, by employing a higher speed ADC, the acquisition time can be decreased by using a higher repetition rate MLL.

In conclusion, we demonstrate a photonic architecture for RF×PRBS mixing with photonic time-stretching, optical integration of the mixed product, and single-shot detection at the output to enable high-speed compressed sensing of sparse-frequency RF signals. The experimental RF detection bandwidth is greater (to our knowledge) than in any previously demonstrated microwave photonic CS system, and the architecture offers significant flexibility for adding more PRBS features (N) and sensing

bandwidth. Signal acquisition for this system is 5–6 orders of magnitude faster than previously demonstrated compressed sensing utilizing wavelength-to-time mapping, and the use of photonic time-stretching permits detection of sparse-frequency RF signals over a much broader bandwidth than would traditionally be possible with the employed electronics alone. The demonstrated system is highly promising for the rapid characterization of sparse and ultrawideband RF spectra as well as the characterization of ultrawideband RF signals with rapid temporal dynamics.

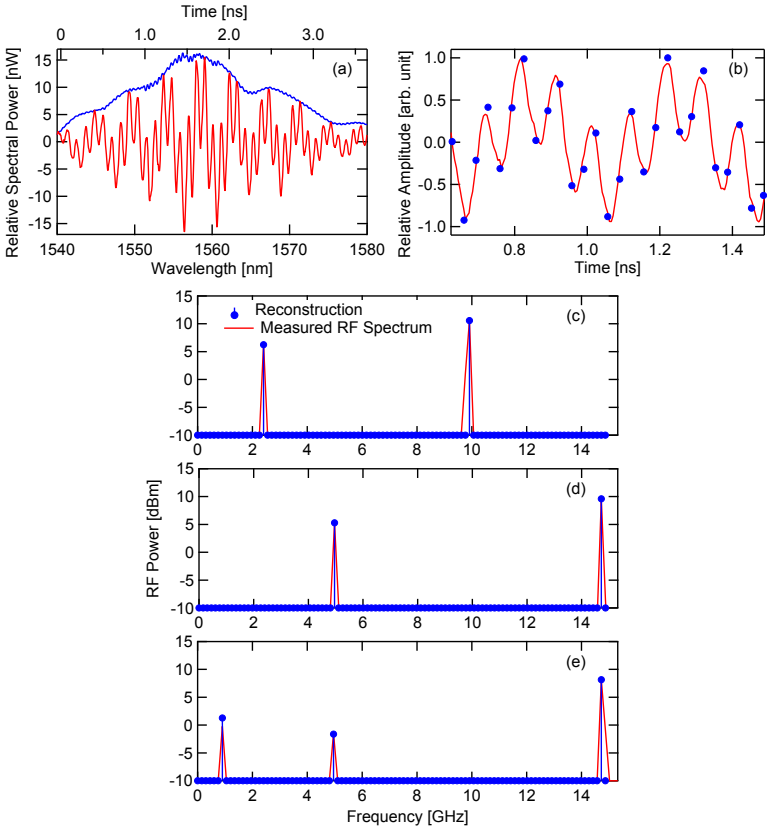

Figure 2.3: (a) Temporal RF measurement derived from the difference in optical spectrum with and without RF modulation shown spectrally due to wavelength-to-time mapping (red curve). The envelope from the spectral shape is overlaid for reference (blue curve). (b) Temporal RF measurement with the effect of the envelope removed and the reconstruction from the RF spectrum shown in panel (c) overlaid. (c) Two-tone reconstruction of peaks at 4.95 and 14.76 GHz, with $N = 100$, $M = 23, \tau = 0.04$, and MSE $= 0.00031$. (d) Two-tone reconstruction of peaks at 2.43 and 9.90 GHz, with $N = 100$, $M = 28, \tau = 0.068$, and MSE $= 0.00072$. (e) Three-tone reconstruction of peaks at 900 MHz, 4.95 and 14.76 GHz, with $N = 100$, $M = 38$, $\tau = 0.05$, and MSE $= 0.00056$.

Chapter 3

Time-Dependent RF Sensing

Here, we extend the chirp procesing approach to photonic CS to measuring arbitrary frequencies and achieve vastly improved frequency resolution and compression. Using joint sparsity reconstruction, we demonstrate experimental acquisition of multi-tone signals at arbitrary frequency offsets from the reconstruction grid. We achieve broad sampling bandwidth well beyond that of the electronics and all-optical integration permitting tremendous reduction in the necessary electronic sampling rate. We demonstrate a photonic system for pseudorandom sampling of multi-tone sparse radio frequency (RF) signals in an 11.95 GHz bandwidth using $< 1\%$ of the measurements required for Nyquist sampling.

3.1 RF Sensing at Arbitary Frequencies

Rapid wideband RF spectrum estimation is a critical technology for applications such as cognitive radio and electronic warfare. However, efficiently detecting spectrum usage across a wide bandwidth is a primary challenge for such systems [43]. Conventional electronic sampling at the Nyquist rate followed by a discrete Fourier transform (DFT) provides a straightforward method of spectrum estimation, but ADCs to cover several 10s of GHz of bandwidth are prohibitively expensive and power hungry, limited in SNR, or unavailable. Thus, there is great interest in applying compressed sensing (CS), which permits recovery of signals from a highly sub-Nyquist number of measurements, to this problem [44].

Photonic systems, which possess extremely large instantaneous bandwidth, are promising for implementing wide-bandwidth RF CS systems. Sampling of a single 1 GHz RF tone in a 5 GHz bandwidth using a PRBS-modulated CW laser and RF low-pass filter was achieved at 5% of the Nyquist sampling rate in [34]. Multiple works have since extended the use of optical signal processing in CS RF sampling. In [45] four CW wavelengths were multiplexed, PRBS modulated, precisely delayed, and demultiplexed after RF modulation into four PDs and ADCs to recover 20 tones in a 5 GHz bandwidth using 120-MHz received bandwidth. In [46] four CW lasers and dispersion compensating fiber were utilized for optical integration of the PRBS-RF product to recover three tones in a 2.5 GHz bandwidth down to 10% of the Nyquist sampling rate. Photonic time-stretch using mode-locked lasers (MLL) and dispersion

management in optical fiber [47–49] has been successfully employed to extend the effective sampling rate beyond the PRBS modulation rate, but so far only tones at harmonics of the laser repetition rate have been reconstructed [37, 50].

The photonic CS approaches above demonstrate accurate reconstruction for signals placed on a frequency grid determined by the system and reconstruction basis. However, for realistic input signals $x(t)$ at arbitrary frequencies, even a small offset of a few parts-per-million from the $\Delta = f_s/N$ frequency grid results in significant squared-error with numerous spurious tones in ideal, noiseless reconstructions [51]. This problem is described as sensitivity to basis mismatch and proposed solutions require modification of the signal model and the DFT sparsifying basis [52, 53]. Basis mismatch was experimentally observed in photonic links, exhibiting up to 100% frequency identification failure for input frequencies near the midpoints of the frequency grid [54]. Several algorithms have recently shown promise in mitigating the errors induced by basis mismatch [55–58]. Alternatively, photonic multi-coset nonuniform sampling allows reconstruction of arbitrary RF signals using a sub-Nyquist acquisition rate, but the technique required the Nyquist number of samples, corresponding to much longer acquisition time at the reduced sampling rate [59].

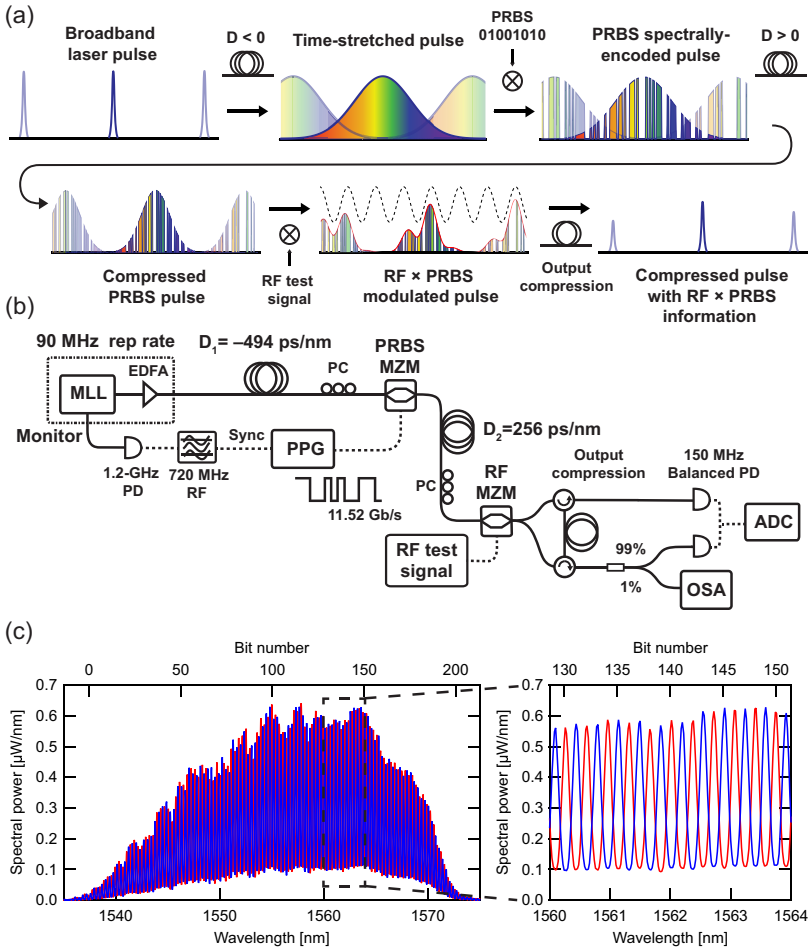

Figure 3.1: (a) Conceptual operation, (b) detailed schematic, and (c) example spectra of 0101... and 1010... patterns.

3.2 Experimental System

The system (Fig. 3.1) functions by time-stretching 300-fs MLL pulses ($f_{\text{rep}} = 90$-MHz repetition rate) in a normal dispersion fiber ($D_1 = -494$ ps/nm) to achieve wavelength-to-time mapping. The pulses are then modulated with PRBS patterns at a rate of 11.52 Gbit/s by a Mach-Zehnder intensity modulator (MZM) driven by a pulse pattern generator (PPG) synchronized to the MLL. The high peak power of the

input pulse train couples with the moderate nonlinearity ($\gamma = 3.8\ \mathrm{W^{-1}km^{-1}}$) and high dispersion of the chirping fiber to produce spectrally-broadened pulses spanning 35 nm and greater than 17 ns in time before PRBS modulation. The stretched duration of the pulses permits 200 features over the full width of the spectrum (Fig. 3.1(c)).

After PRBS modulation, the pulses are partially compressed in an anomalous dispersion fiber ($D_2 = 256$ ps/nm), increasing the effective sampling rate by a factor of $D_1/(D_1 + D_2) = 2.07$. Since the temporal compression ratio is enabled by well-defined fiber dispersion, we have found the effective sampling rate to be consistent across many days of measurements without any stabilization. Measurements can be acquired indefinitely as long as the laser remains stably mode-locked. The partially compressed pulses are modulated by the RF signal in a dual-output MZM. The two outputs are represented as $[1 + \alpha x(t)]p'(t)$ and $[1 - \alpha x(t)]p'(t)$ where $p'(t)$ is the compressed PRBS waveform and α is the RF MZM modulation depth. Finally, the residual chirp is compensated using circulators and a common fiber ($D = 238$ ps/nm) to restore both arms to nearly transform-limited duration. One arm is tapped with a 99:1 coupler and input to an optical spectrum analyzer (OSA) to characterize the shape of the $p(t)$ patterns on the spectrum and calibrate the sensing matrix $\mathbf{\Phi}$ matrix [50]. A 150-MHz balanced photodetector (PD) computes the difference between the two arms, producing a pulsed voltage waveform with peak values proportional to $\int_{t_0}^{t_1} 2\alpha x(t)p'(t)\mathrm{d}t$ where t_0 and t_1 are the temporal bounds of the partially compressed PRBS pulses. This doubles the signal level, suppresses laser noise, and eliminates

the need for an unmodulated reference to digitally compute a difference signal. To reach the maximum data compression ratio, we employ a synchronized ADC clocked at the laser repetition rate with its sampling windows aligned to the peaks of the output voltage waveform. In this way, the required sampling rate to reconstruct the sparse input signal is reduced by a factor of 266.

In other photonic realizations of the random demodulator, the integrator was implemented with a low-pass electronic or microwave photonic filter [34,45,46], which is difficult to approximate as an ideal integrator for 100-MHz or GHz sampling rates [60]. This problem is solved in our approach because after the two modulation stages, the pulse is restored to a ∼ps duration and acts as an impulse to the PD such that a single ADC sample can represent the full inner product.

At the PRBS modulation stage, the pulse duration is longer than the 11.1-ns repetition period and the tail of each pulse overlaps the head of the succeeding pulse. Thus, after modulation, the pulses share certain pattern segments, but these features are located at completely different wavelengths and upon partial-compression there is no temporal overlap of the shared segments or of the pulses, maintaining the orthogonality between the rows of pseudorandom $\mathbf{\Phi}$ matrix. After partial compression, the sampling duty cycle (T) is determined by the optical bandwidth and dispersive design: $T = |D_1 + D_2|\Delta\lambda f_{\text{rep}}$. Here the parameters were chosen to balance the RF bandwidth and the duty cycle ($T = 0.75$). The unobserved period within each pulse repetition window corresponds to only 2.7 ns, which is sufficiently

small for the observation of spectrally sparse carriers with each individual carrier bandwidth up to the order of 100 MHz.

The present system can be scaled to effective sampling rates beyond the electronic pattern rate by a factor up to 10× or more [61] by ensuring sufficient optical bandwidth per PRBS bit slot δt at the increased rate: $\delta t^2 > |D_1 + D_2|\lambda^2/c$ [7]. This can be achieved without gaps in the sampling waveform by decreasing D_1 and time-interleaving the PRBS pulses with relative delays equal to several pulse periods. In this way, a continuous train of minimally correlated pseudorandom patterns at an extremely high rate can be constructed.

3.3 Reconstruction Algorithm

To reconstruct the signal under test, the random demodulator CS framework [35] models a sparse-frequency input as a Fourier series $x(t) = \sum_{n=-N/2}^{N/2-1} X(n) e^{j\frac{2\pi}{T_x}nt}$, where T_x is the period of $x(t)$ and N is a positive even integer representing the full dimension of the discrete signal. The finite summation indicates that the signal is assumed to be bandlimited in the range $-0.5W \leq \frac{n}{T_x} \leq 0.5W$ where n is an integer and W is the PRBS rate, often referred to as the chipping frequency. The input $x(t)$ is assumed to be K sparse, which denotes that only $K \ll N$ of the coefficients $X(n)$ are non-zero. PRBS measurement signals are chosen to satisfy the restricted isometry

property (RIP), preserving the Euclidean length of K sparse signals and permitting recovery from a sub-Nyquist number of measurements.

The input signal $x(t)$ is mixed with the PRBS signal $p(t)$ and fed into an ideal integrator and sampled at a constant rate R where W/R is an integer. The mixing and integrate-and-dump process can be cast as a matrix multiplication $\mathbf{y} = \mathbf{\Phi x}$ where, for M linear pseudorandom measurements, $\mathbf{\Phi}$ is an $M \times N$ matrix of the form

$$\mathbf{\Phi} = \begin{bmatrix} p_0 \dots p_{\frac{N}{M}-1} & & & \\ & p_{\frac{N}{M}} \dots p_{\frac{2N}{M}-1} & & \\ & & \ddots & \end{bmatrix} \tag{3.1}$$

and $N/M = W/R$. A CS recovery algorithm is employed to find the sparsest representation $\mathbf{s} = \mathbf{\Psi x}$ of the input signal, constrained by the empirical measurement $\mathbf{y} = \mathbf{\Phi \Psi^{-1} s}$ where $\mathbf{\Psi}$ is an appropriate sparsifying matrix, i.e., a discrete Fourier Transform (DFT) matrix for sparse frequency signals.

Our previous work in chapter 2 [50] restricted the input RF frequencies to multiples of the laser repetition rate f_{rep}. The measurement matrix thus took the form

$$\mathbf{\Phi} = \begin{bmatrix} p_0 \dots p_{N-1} \\ p_N \dots p_{2N-1} \\ \vdots \end{bmatrix}. \tag{3.2}$$

This simplifies reconstruction by eliminating the possibility of phase slip $\Delta\phi = 2\pi f_{\mathrm{RF}}/f_{\mathrm{rep}}$ for an arbitrary frequency f_{RF} between successive measurement windows. However, the full dimension N of the reconstructed signal was fixed at the number of features per pattern (100 in that realization). By considering the passage of time between individual pseudorandom measurements (i.e., shifting horizontally the rows in $\mathbf{\Phi}$) in the random demodulator framework, N can be increased as desired by increasing the number of measurements M. Here, this affords an increase in the dimension of the reconstructed frequency grid by a factor of 250.

To reconstruct arbitrary RF tones with random offsets from the discrete basis frequencies, we take the approach of solving a joint sparsity minimization with simultaneous orthogonal matching pursuit (SOMP) [62]. The original observation vector of length M is subsampled with replacement to generate C shorter observation vectors of length L, where $L < M$. In this way, the accumulated phase shift across multiple pseudorandom measurements between the input tones and the closest DFT basis frequency can be reduced (for illustration, see [52]). Each of the C sampling channels is expected to yield the same sparse set of basis vectors, but with different coefficients s magnitude-wise. Most importantly, we expect the support of s to be consistent across multiple observations. Thus, we employ a similar strategy to that of bagging or bootstrap aggregating, popular in the machine learning community, to generate C multiple-measurement observations from our M collected measurements via random sampling with replacement and then solve the sparse recovery problem via SOMP.

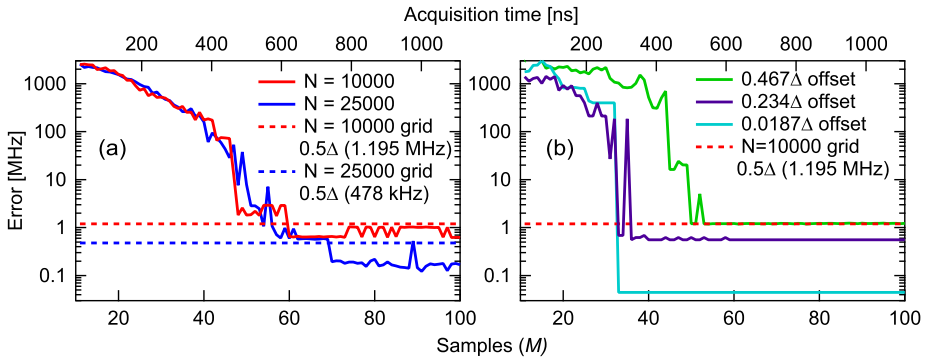

Figure 3.2: (a) Average frequency error when reconstructing a single RF frequency at nominal input frequencies of 500 MHz to 10 GHz in 500 MHz increments. (b) Average reconstruction error for frequencies at three offsets from the $N = 10000$ reconstruction grid with Δ spacing: 2.5 GHz (0.0187Δ offset), 4.5 GHz (0.234Δ offset), and 9.0 GHz (0.467Δ offset). $L = 10$, and $C = \text{round}(M/3)$.

3.4 Experimental Results

To demonstrate the system performance, we first consider the frequency accuracy when reconstructing a single input tone within the system bandwidth. Figure 3.2(a) shows the rapid convergence of the reconstructed frequency, averaged over 20 trials of 20 single-tone inputs at nominal frequencies from 500 MHz to 10 GHz with 500 MHz spacing. As in [54], we consider the two nearest grid frequencies to the actual frequency to be correct identification. The recovered error quickly diminishes to below the mean error of 1/2 of the grid spacing: 1.195 MHz for $N = 10000$ points and 478 kHz for $N = 25000$ points on a two-sided bandwidth of 2×11.9505 GHz. This implies perfect frequency identification at $M = 60$ measurements for $N = 10000$ (0.6% of Nyquist) and $M = 70$ for $N = 25000$ (0.28% of Nyquist). Figure 3.2(b) shows the convergence of 20 trials of three frequencies at nominal distances of 0.0187

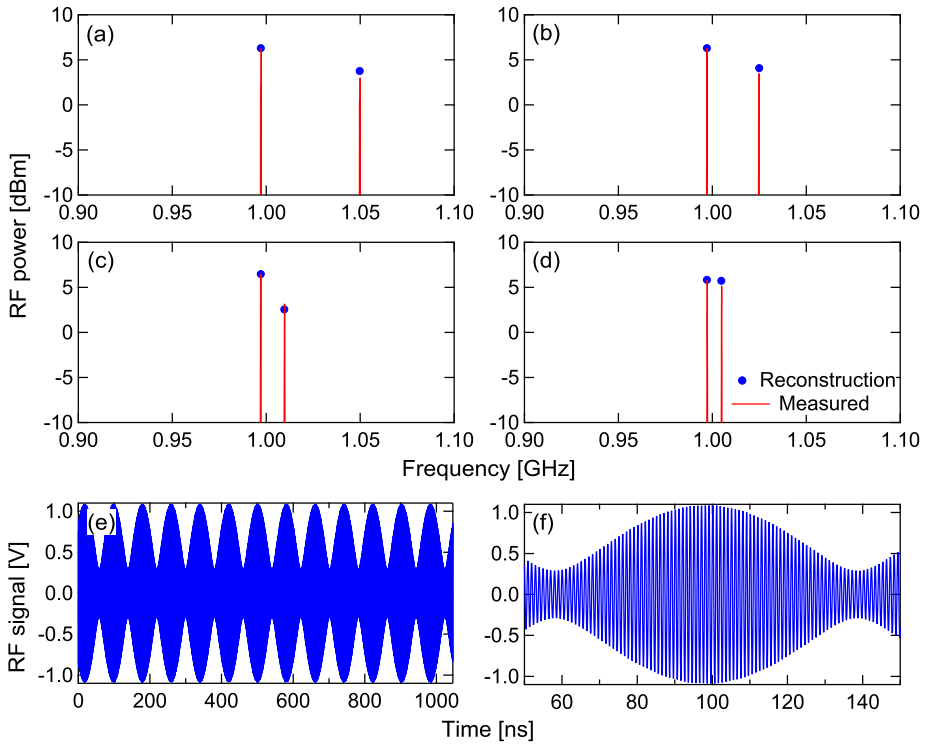

Figure 3.3: Reconstructions and measured RF spectra of closely-spaced tones near 1 GHz at separations of (a) 53 MHz, (b) 28 MHz, (c) 13 MHz, and (d) 8 MHz. (e) Full and (f) expanded time domain reconstruction from (c). $M = 100$, $N = 25000$, $L = 20$, and $C = 30$.

(2.5 GHz case), 0.234 (4.5 GHz case), and 0.467 (9.0 GHz case) times the grid spacing Δ from the $N = 10000$ frequency grid. The tones nearer to a sampling grid point converge faster, but all cases converge rapidly with fewer than $M = 60$ measurements. The acquisition time for convergence at both values of N is nearly equal to the time required by a conventional ADC and FFT. The convergence of the 9.0 GHz tone ($\Delta = 0.467$) is a significant improvement over conventional recovery in [54] where the support was never found correctly for offsets close to 0.5 times the grid spacing.

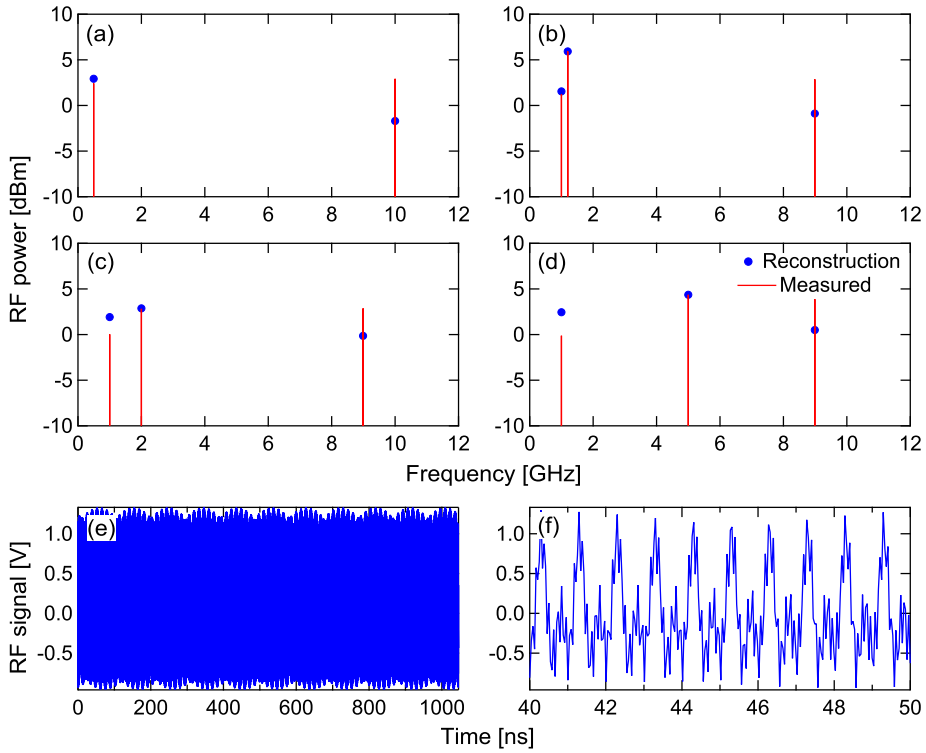

Figure 3.4: Two- and three-tone reconstructions. (a) 497 MHz and 10.00 GHz; (b) 1.00, 1.20, and 8.99 GHz; (c) 1.00, 2.00, and 8.99 GHz; (d) 1.00, 5.00, and 8.99 GHz. (e) Full and (f) expanded time domain reconstruction from (c). $M = 200$, $N = 25000$, $L = 20$, and $C = 60$.

Figure 3.3 shows the ability to discriminate between two closely-spaced tones without erroneous spurs. One tone is fixed at 997 MHz and a second tone is brought successively closer at distances of 53, 28, 13, and 8 MHz. Perfect frequency identification and excellent agreement between the measured and reconstructed amplitude are achieved in all cases with $M = 100$ measurements and an $N = 25000$ frequency grid (0.4% of Nyquist).

Figure 3.4 shows the ability to identify two- and three-tone RF signals across an 11.95 GHz bandwidth utilizing less than 1% of the measurements traditionally

required for Nyquist sampling. Perfect frequency identification of each tone was achieved in all cases with $M = 200$ measurements and an $N = 25000$ frequency grid (0.8% of Nyquist). Though, for most applications, correct identification of active frequencies is most important, we expect that better amplitude agreement over the full system bandwidth can be achieved with better modeling of the frequency responses of the optoelectronics.

In conclusion, we have demonstrated accurate frequency identification of single and multi-tone RF signals at arbitrary frequencies using less than 1% of Nyquist sampling. Our chirp processing approach permits an effective sampling rate 2.07× the electronic pseudorandom modulation rate as well as optical integration of the PRBS-RF inner products to reduce the necessary analog-to-digital conversion rate by a factor of 266. Joint-sparsity reconstruction with SOMP via a simple observation bagging strategy, permits accurate reconstruction of frequencies at random offsets from the reconstruction frequency grid.

Chapter 4

Continuous High-Rate Photonically-Enabled Compressed Sensing (CHiRP-CS) Microscopy

We demonstrate in this chapter an imaging system that harnesses continuous high-rate photonically-enabled compressed sensing (CHiRP-CS) for image acquisition. As before, ultrahigh-rate spectral shaping is achieved through dispersive chirp processing of broadband laser pulses, but in the CHiRP-CS imaging approach these pulses serve as ultrafast structured illumination of objects flowing through a one-dimensional (1D) field of view. We investigate two different 1D spatial dispersers for low and high magnification imaging of complex test objects printed on transparencies and 25-μm polystyrene microsphere clusters, respectively, placed on

a spinning hard disk platter. Compressive measurements are acquired continuously without averaging at a rate of one digital sample per optical pulse. We demonstrate successful reconstruction of 2D images from the 1D compressive measurements at effective 1.46, 4.19, and 7.32-Gigapixel/sec rates from a 90-MHz sampling rate. We also extend the system with optical pulse interleaving to 9.9, 19.8 and 39.6-Gigapixel/sec rates from a 720-MHz acquisition rate.

4.1 Flow Cytometry

Flow cytometry (FC) is an indispensable tool for single-cell characterization and sorting of very large heterogeneous populations of up to millions of cells. It is very widely used throughout basic cell and molecular biology, genetics, immunology, and environmental science to quantify the phenotypes and physiological responses of single cells [63,64]. In a typical flow cytometer, biological samples in suspension pass through a flow cell to an interrogation point with one or several laser beams focused to a spot slightly larger than the cells, typically 10 microns in diameter. Hydrodynamic focusing in the flow cell forces sample particles into a single file line in the center of the laser illumination. Detection optics collect forward scattered light (FSC) along the beam direction and 90 deg to the side of the beam (side scattered light, SSC) onto photodetectors to estimate the size of cells (FSC) and the granularity or internal complexity (SSC). To gain additional information about cell biochemical properties,

multiple fluorescent probes are frequently employed and the SSC emission spectrum separated with a bank of dichroic mirrors and separate photomultiplier tubes. Typical FC systems employ up to 5 to 10 channels for detecting fluorescence, but higher numbers have been demonstrated [65]. Because sensitive high-speed photodetectors and analog-to-digital converters (ADC) are widely available, FC systems capable of analysis at rates up to the order of 100,000 cells/second in flows up to 10s of m/s (at the interrogation point) have been available for a few decades now. The technique and its extension with microdroplet electrostatic sorting are now more than 50 years old.

Because of its capacity for high analysis rates, FC is a compelling technique to permit the detection and characterization of rare and ultrarare cells with incidence rates of parts per million or below that are important to many basic and clinical problems in biology such as isolation of rare cell clones with specific mutations, rare metastatic cells, and rare stem/progenitor cells [66, 67]. Circulating tumor cells (CTCs) in the bloodstream are rare cells of particular interest that have been correlated with metastatic disease, which causes the majority of cancer-related deaths [68]. In addition to the statistical sampling difficulties of locating rare positive cells in a sea of uninteresting negative cells, FC inevitably encounters a problem of signal-to-noise in the cell labeling process [66]. It is very difficult to make probes that will bind specifically to only the cells of interest so multiple probes are most commonly employed in order to discriminate between truly interesting cells and uninteresting cells that will nonetheless pick up some of the rare cell probe. More

probes are frequently required as cells of interest become more rare. High speed becomes paramount when taking into consideration not only the instrument stability, but also the marker stability and the cell viability.

Imaging flow cytometry (IFC), represented by devices such as the Amnis ImageStream^X, replaces the photomultipliers of conventional FC with two multichannel charge-coupled device (CCD) cameras such that multiple 2D fluorescence images can be acquired of each cell in the flow, greatly increasing the information content gained per cell [69]. 2D imaging in flow provides much more information about morphology and localization of fluorescence compared to FC and permits assays, for example, of nuclear translocation, apoptosis, colocalization of markers, and intracellular trafficking [70]. The technique is well-suited to identifying rare cells unambiguously, but the addition of high sensitivity time delay integration CCD cameras strictly limits the reasonable flow speeds to 0.06 m/s to prevent motion blurring of the images [71]. Thus, IFC is limited to analysis rates up to approximately 1000 cells/second, which severely limits the possibilities for detection of rare cells within practical time constraints (or time constraints imposed by active biological processes of interest). Both IFC and other high content screening (HCS) techniques typically based on automated microscopy of microwell arrays are considered to be orders of magnitude too slow for many studies in combinatorial biology [72]. And both generate terabytes of image information very quickly even at slower than desired maximum analysis rates.

4.2 High-Speed Imaging

Ultrahigh-speed continuous imaging is a critical technology for high-throughput screening of cell structure and behavior [73], drug discovery [74, 75], rare cell detection for cancer diagnostics [76], and numerous other clinical and basic research applications throughout the life and physical sciences [77, 78]. For example, understanding cellular heterogeneity has become essential for investigating drug resistance in cancer treatment wherein cells of interest often comprise less than 0.2% of the total population [78]. Identification and isolation of subpopulations presents a significant challenge for statistically and biologically meaningful analysis and thus demands techniques capable of both high throughput and high information content.

Photonic ultrafast microscopic imaging approaches have recently shown promise in closing the gap in analysis rates between high information content IFC and high throughput traditional FC. Time-stretch microscopy replaces continuous wave illumination sources with a broadband ultrafast laser source that can be imaged onto a 1D spectral line using a dispersive element [76, 79–84]. Objects of interest pass through the wavelength-mapped confocal line, imprinting their spatial information onto the spectra of the pulses. By collecting the spatially-patterned pulses into an optical fiber and applying large amounts of fiber-based chromatic dispersion and optical amplification (see section 1.1.2 and 1.1.5), it is possible to map the pulse wavelengths to time and read out the spatial information serially with a single photodetector and ultrahigh rate ADC. By employing ultrafast lasers and fiber-based information

processing, time-stretch microscopy elegantly solves the issue of low signal level at high frame rates with corresponding short integration times and the problem of motion blur that makes even the fastest continuous readout CCDs unusable for fast microscopic flows. Time-stretch microscopy permits shutter speeds in the range of 10 ps, much faster than the 0.5–1 μs integration times of the fastest continuous readout CCDs. Imaging of cells in microfluidic flows moving up to 10 m/s with resolution down to 1.2 μm has been reported [82].

The first demonstration of rare cell detection using photonically-enabled microscopy detected the MCF7 cell line (breast cancer) spiked in blood: the cells were fixed with formaldehyde and coated with metal beads with a diameter of 1 μm via an antibody to EpCAM [76]. After this coating, it was possible to identify the cancerous cells down to an incidence of one part-per-million at a rate of 100,000 cells/second in the presence of white blood cells, residual red blood cells after the sample was lysed, and free-floating metal beads. A conventional flow cytometer, by contrast, would achieve 100× lower detection specificity due to the similarity in the scattered light and fluorescence intensity in an equivalent analysis. Compared to the Amnis ImageStream^X, the device was predicted to be capable of detecting rare cells on the order of 1 in 10 million within a few minutes rather than weeks at the latter's lower analysis rate.

4.3 Performance Trade-Offs

High-speed imagers generally fall into two categories: burst sampling and continuous sampling. Using in situ storage, cutting-edge complementary metal-oxide semiconductor (CMOS) [85] and CCD [86] imaging arrays have achieved impressive burst frame rates of 10s of MHz [87]. However, these architectures offer maximum record lengths limited by pixel-level memory constraints to approximately 100 frames. Microscopic imaging up to a 4.4 THz frame rate for 6 frames has been demonstrated in a technique called sequentially timed all-optical mapping photography (STAMP), using spectrally-carved mode-locked laser pulses spatially separated on an imaging array using a diffraction grating [88]. Burst imaging of macroscale objects at up to 100 GHz frame rates for up to 350 frames using a digital micromirror device (DMD) and streak camera in conjunction with compressed sensing (CS) recovery has also been recently demonstrated in a technique named compressed ultrafast photography (CUP) [29]. The STAMP and CUP burst sampling systems achieve incredible burst pixel rates of 1.66 exapixels/sec and 2.25 petapixels/sec, however these sampling rates can only be sustained for time spans of 1.37 ps and 3.5 ns respectively, followed by dead times of at least 1–10 ms for the required image sensor readout.

While burst sampling systems are useful for observing extremely fast but isolated events in a single-shot, many applications (e.g. high-throughput diagnostics) necessitate continuous sampling, which requires tremendous hardware resources to record the massive stream of high-speed image data. Recently, cutting-edge imaging archi-

tectures employing ultrafast laser pulses and fiber-optic-based information processing yielded a performance leap in ultrahigh-speed continuous acquisition [79, 80, 82–84]. Still, such approaches remain fundamentally limited in speed, resolution, and image quality by the measurement rate of electronic digitizers [89]. For example, both traditional CCD arrays and state-of-the-art photonic systems such as serial time-encoded amplified microscopy (STEAM) read out the pixel information serially with a single analog to digital converter (ADC). Thus the number of pixels acquired per second is equal to the sampling rate of the ADC.

Notably, real signals such as most natural images are highly compressible and contain far less information than their full capacity as evidenced by the prevalence of modern data compression technology. Moreover, compressed sensing indicates that, due to their compressibility, real signals can be acquired with far fewer measurements than conventionally deemed necessary [23,25,26,30,90]. Thus cutting-edge ultrahigh-speed imaging systems are inefficient, collecting far more data than is required to accurately characterize the signals of interest and thus limiting their potential operating rate.

Recently, data compression in the optical domain has become a popular topic of research to improve analog-to-digital conversion efficiency. As discuessed in chapters 2 and 3, several systems have been demonstrated for compressive photonic sampling of sparse radio frequency (RF) signals [34, 37, 45, 50, 91]. Beyond permitting signal characterization with a sub-Nyquist number of measurements, compression in the optical domain has also enabled extension of the effective sampling band-

width beyond the electronic subsystem limitations [37, 50] and temporal integration of the pseudorandom measurements to allow for low ADC sampling rates [50, 91]. In addition to compressive sampling, the anamorphic stretch transform (AST) has been proposed to achieve time-bandwidth compression of pulsed optical waveforms by employing sublinear group delay chirping in conjunction with measurement of the complex electric field [92, 93]. Very recently, multiple groups have also shown interest in compressed sensing imaging using ultrafast pulses [94–97], but to our knowledge this work is the first demonstration of ultrafast structured illumination imaging of microscopic objects moving at high speed.

4.4 Compressed Sensing Imaging

Real images and most real-world signals are highly compressible and can be accurately represented by relatively few significant coefficients in an appropriate mathematical basis. Sparse approximation—the process of transforming the signal to this basis and saving the most significant coefficients while ignoring the rest—is the foundation of modern data compression technologies such as the Joint Photographic Experts Group (JPEG) and Moving Picture Experts Group (MPEG) formats [98, 99]. Traditionally a signal is sampled according to the Nyquist theorem to acquire a raw digital representation and then a compression algorithm is applied, eliminating as much of the redundancy in the original data as possible. Hence, most of the acquired

data is simply thrown away. Consequently, for most applications in high-speed continuous acquisition, the raw image data bandwidth is far larger than is truly necessary.

Compressed sensing is a recent and influential sampling paradigm that advocates a more efficient signal acquisition process. According to CS theory, a K-sparse signal $\boldsymbol{x}^\star \in \mathbb{R}^n$ is measured through a set of M measurements of linear projections $y_i = \langle \boldsymbol{a}_i, \boldsymbol{x}^\star \rangle$, $i = 1, ..., M$, in which vectors $\boldsymbol{a}_i \in \mathbb{R}^N$ form the matrix $\boldsymbol{A}$ of size $M \times N$. To reconstruct $\boldsymbol{x}^\star$, ℓ_1-minimization is proposed to solve the following problem

$$\min_{\boldsymbol{x}} \|\boldsymbol{x}\|_1 \quad \text{s. t.} \quad \|\boldsymbol{y} - \boldsymbol{A}\boldsymbol{x}\|_2 \leq \sigma. \tag{4.1}$$

The case above deals with imperfect observations contaminated by noise, i.e., $\boldsymbol{y} = \boldsymbol{A}\boldsymbol{x}^\star + \boldsymbol{w}$ where $\boldsymbol{w}$ is some unknown perturbation bounded by a known amount $\|\boldsymbol{w}\|_2 \leq \sigma$. If the sensing matrix $\boldsymbol{A}$ obeys the Restricted Isometry Property (RIP) [25] and σ is not too large, then the solution $\hat{\boldsymbol{x}}$ of Eq. (4.1) does not depart significantly from the optimal solution $\boldsymbol{x}^\star$, so long as the number of measurements M is on the order of $K \log N$ [23,25,26,30,90]. Thus the CS framework advocates the collection of significantly fewer measurements than the ambient dimension of the signal ($M \ll N$).

A notable CS imaging architecture is the single-pixel camera in which light collected from an object is randomly combined via a digital micro-mirror device (DMD) before it is focused onto a single-pixel photodetector [31]. By tuning each micro-mirror in the pixel array, the system creates pseudorandom 2D patterns that modulate the

image before summing the optical power using the single detector, thereby optically performing the inner product, $y_i = \langle \boldsymbol{a}_i, \boldsymbol{x}^\star \rangle$. This technique has also been extended to macroscopic [100] and microscopic structured illumination imaging [101]. However, in all of these systems the need to mechanically transition the MEMS-actuated micromirrors sets the upper limit of the pattern rate to a few kHz, restricting the total image acquisition time. In contrast, the CHiRP-CS architecture we demonstrate here achieves illumination pattern rates more than 20,000× faster. Thus our approach allows for application of CS to the domain of ultrahigh-speed image acquisition.

4.5 Experimental System

The principle of operation of the CHiRP-CS imaging system (Fig. 4.1) is to modulate pseudorandom patterns at an ultrahigh rate onto the optical spectra of broadband mode-locked laser pulses and then utilize these spectral patterns to create structured illumination of an object. Light collected from the object is directed onto a single-pixel high-speed photodetector and the energy of each returned laser pulse is recorded continuously by a synchronized real-time ADC. A CS recovery algorithm then constructs an image of the object from far fewer measurements than would be required for conventional Nyquist sampling.

Spectral patterning is accomplished using chirp processing in optical fiber [50]. A passively mode-locked erbium-doped fiber laser (MLL) emitting 300-fs pulses at

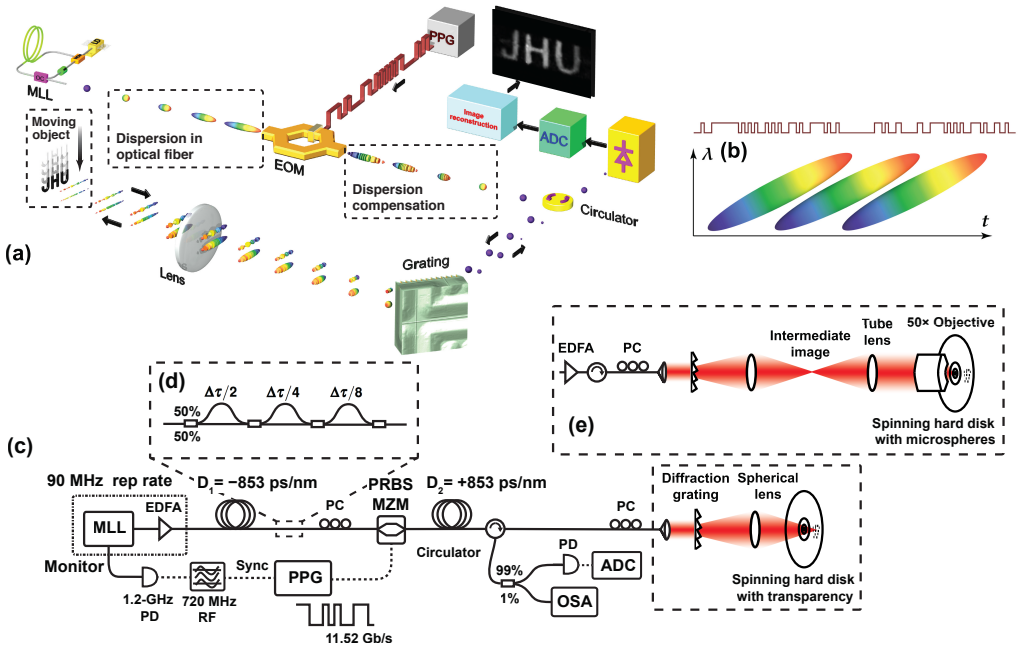

Figure 4.1: (a) Broadband laser pulses are dispersed in optical fiber to accomplish spectrum-to-time mapping. Each pulse is modulated with a unique ultrahigh-rate pseudorandom binary pattern and then re-compressed in fiber (Dispersion compensation) to an ultrashort duration before passing through a 1D wavelength-to-space mapping diffraction grating and lens that focuses the spectral pattern onto the object plane, providing structured illumination of the object flow. The output pulse energy traveling back through the spatial disperser to the photodiode and ADC represents an optically-computed inner product between the pseudorandom pattern and the object. The image is reconstructed via a sparsity-driven optimization from sub-Nyquist compressive measurements. (b) Temporal overlap of the pulses at the pattern modulation stage. (c) Detailed system schematic for low magnification results in Subsection 4.7.1. (d) Pulse interleaver and (e) spatial disperser with microscope for high magnification results in Subsection 4.7.2.

the native 90-MHz repetition rate (centered at 1555 nm) is used in conjunction with a C-band erbium-doped fiber amplifier (EDFA) to amplify the optical pulse train to 200 mW. Dispersive spectrum-to-time mapping is then performed in a dispersion compensating fiber (DCF) with a total group velocity dispersion (GVD) of -853 ps/nm and dispersion slope of -2.92 ps/nm^2 at 1550 nm. Spectral broadening to a full width of 33 nm is achieved through the high peak power after the EDFA and the moderate nonlinearity ($\gamma = 7.6$ W^{-1}km^{-1}) of the DCF, stretching the 300-fs MLL pulses to greater than 28 ns.

Pattern modulation is achieved with an 11.52-Gbit/s pulse pattern generator (PPG) synchronized to the MLL driving a 20-GHz Mach-Zehnder intensity modulator (MZM). This permits 128 pseudorandom binary features per 11.1-ns pulse repetition period. The PPG can output user-programmable patterns up to 1.3 Mbit in length; in practice a customized string of 1.1 Mbit or 8615 patterns is used. Of these, a few patterns are used as a header to determine the alignment between the samples from the ADC and the predetermined pseudorandom patterns for the reconstruction. The PPG modulates the set of patterns continuously permitting uninterrupted sampling and the 95.7-μs repetition period for the set of patterns does not affect the robustness of the sampling approach.

As depicted in Fig. 4.1(b), the time-stretched pulses overlap partially during pattern modulation. Thus, neighboring pulses share some temporal features, but these features are mapped to different wavelengths and, thereby, involve different regions

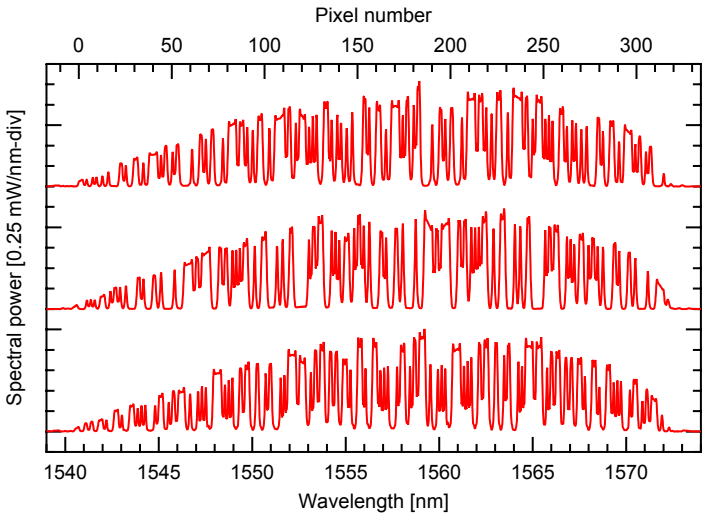

Figure 4.2: Example repeating 128-bit pseudorandom binary patterns observed with an optical spectrum analyzer. In practice, we reconstruct 325 horizontal pixels utilizing the full width of the spectrum. Actual sampling patterns are unique to each pulse and cannot be observed on the averaged spectrum.

of the structured illumination pattern. This preserves mutual incoherence between the pseudorandom patterns while permitting many more features per pulse. Three example PRBS-encoded laser pulse spectra are shown in Fig. 4.2. In practice, we achieve 325 features per pulse within the spectral bandwidth, which sets the horizontal pixel resolution of the reconstructed images.

After spectral patterning, the pulses are time-compressed in standard single-mode fiber (SMF) with complementary GVD of +853 ps/nm and dispersion slope of +2.92 ps/nm^{2}at 1550 nm to the DCF. The spectrally-patterned and compressed laser pulses pass through a 1D spatial disperser to serve as ultrafast structured illumination of an object flow.

CHAPTER 4. CONTINUOUS HIGH-RATE PHOTONICALLY-ENABLED COMPRESSED SENSING (CHIRP-CS) MICROSCOPY

Here we demonstrate the CHiRP-CS imaging system at two levels of magnification and therefore we construct two different 1D spatial dispersers. The low magnification disperser is composed of a 600-line/mm ruled diffraction grating and 123-mm effective focal length spherical lens. The high magnification disperser employs the same grating with a 1-m focal length spherical lens to form an intermediate structured illumination image before a 200-mm tube lens and a 50× near-IR microscope objective (Olympus LCPLN50XIR, NA=0.65) designed for long working distance. Large-area high-resolution optics are specifically chosen to allow the spectral resolution of the diffraction grating to exceed the minimum feature size. To test the system under operating conditions safe for biological samples, we fix the optical power at 300 μW at the object plane.

Each feature occupies a spectral bandwidth of 12.5 GHz, which corresponds to a shutter speed of 35.2 ps for a transform-limited Gaussian feature inside the disperser. The decreased modulation depth for the fastest (e.g., 010 or 101) alternating features (Fig. 4.2) is a product of the single feature bandwidth and the pattern modulation rate. By adjusting the pattern modulation rate, it is possible to achieve >15 dB modulation depth for all features across the full spectral width [50] to approach ideal binary patterns with an envelope corresponding to the spectral shape.

Test objects pass through the focused image of the structured illumination and the scattered light returns through the disperser into an optical fiber and amplified 150-MHz photodetector. Thus, the system behaves as a confocal imager. As in prior work

focusing on application to imaging flow cytometry [76], the objects move through the system field of view at a constant velocity and 2D images are reconstructed with a vertical dimension that corresponds to both time and vertical spatial extent.

The detected pulse energy, recorded with a synchronized ADC, represents the vector inner product between the spatial profile of the object and the unique spectral illumination pattern. Therefore, only one digital sample per pulse, acquired at the laser repetition rate, is required for each compressive measurement. To achieve the minimum electronic digitization rate for the greatest system sampling efficiency, an externally-clocked ADC is driven with a 90-MHz sampling clock derived from the MLL monitor port input to a 1.2-GHz photodiode with appropriate RF bandpass filters. The phase of the sampling clock is fixed to align the sampling windows with the peaks of the detected voltage waveform.

The low magnification disperser produces a 2.77-mm $\times$ 5.4-μm structured illumination line with 8.5-μm $\times$ 5.4-μm features at the object plane. In the high magnification disperser, the tube lens and objective (designed for 180-mm tube length) result in a 55.6$\times$ demagnification of the structured illumination patterns to create 1.2-μm $\times$ 1.2-μm features across a 390-μm 1D field of view. However, in practice, we add a low-power EDFA before the high magnification disperser to compensate the additional coupling loss into the microscope objective. Lower gain in the EDFA at the edges of the spectrum causes slight narrowing of the field of view to 330 μm with 275 horizontal pixels (28-nm spectral width).

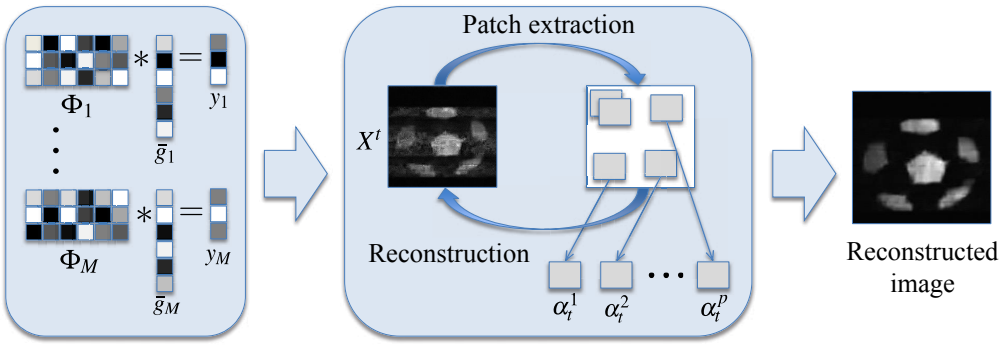

Figure 4.3: Patch based image recovery from 1D compressive pseudorandom measurements, which iterates between two steps—global reconstruction of the image estimates and maximizing the sparsity level of all local image patches.

Finally, to investigate even higher acquisition rates in the high-magnification system, we also add three time-interleaving fiber Mach-Zehnder interferometers after the time-stretching fiber, before the PRBS MZM to increase the pulse repetition rate to 720 MHz (Fig. 4.1(d)). To accommodate the new pulse repetition rate, we also switch to a 1.2-GHz PD and 720-MHz ADC sampling rate.

4.6 Reconstruction Algorithm

To reconstruct the 2D image frames from the 1D compressive pseudorandom measurements, a naïve approach is to recover one image row at a time independently. Instead, we further develop a novel 2D reconstruction algorithm tailored to this imaging apparatus. As depicted in Fig. 4.3, we utilize ℓ_1-minimization coupled with a discrete cosine transform (DCT) basis at the local level of blocks of pixels called patches: any selected local patch should be sparse. Out of all candidate images

that are consistent with the 1D measurements, the iterative optimization algorithm seeks the most sparse set of overlapped patches.

Similar to conventional image compression such as JPEG, the reconstruction framework focuses on the local image structures. A popular model to quantify local image information is sparsity in an appropriate domain: given a patch or block of pixels $x \in \mathbb{R}^{N_b \times M_b}$ extracted at random location from an image, the coefficient $\alpha \in \mathbb{R}^{N_b \times M_b}$ of x under some sparsifying transform $\tilde{\Psi}(\cdot)$ defined by

$$\alpha = \tilde{\Psi}(x)$$

should be sparse or compressible.

The recovery process estimates the set of sparse coefficients $\{\alpha^k\}_{k=1}^p$ of the patch set $\{x^k\}_{k=1}^p$ covering the entire image of interest which is consistent with the 1D observations. Denoting $\{\bar{\alpha}^k\}_{k=1}^p$ as the sparse coefficients of the patches $\{\bar{x}^k\}_{k=1}^p$ extracted from the original image $\bar{G} \in \mathbb{R}^{N \times M}$, the 1D compressive measurement process can be written as

$$y_j = \Phi_j[P(\{\Psi(\bar{\alpha}^k)\}_{k=1}^p)]_j, \ \forall j = 1, ..., M$$

where $\Psi(\cdot)$ is the inverse sparsifying transform of $\tilde{\Psi}(\cdot)$ satisfying $\bar{x}^k = \Psi(\bar{\alpha}^k), \ \forall k = 1, ..., p$; $P(\cdot)$ is the operator that combines the set of image patches $\{\bar{x}^k\}_{k=1}^p$ back to the original image, i.e., $\bar{G} = P(\{\Psi(\bar{\alpha}^k)\}_{k=1}^p)$; $\Phi_j \in \mathbb{R}^{m \times N}, \ \forall j = 1, ..., M$,

is the local pseudorandom sensing matrix used to measure row $\bar{g}_j$ of $\bar{G}$ and y_j is the corresponding measurement vector. Given the set of measurement vectors and sensing matrices $\{(y_j, \Phi_j)\}_{j=1}^{M}$, we propose to obtain the sparse coefficients from the following optimization problem

$$\begin{aligned} \min_{\{\alpha_k\}} \quad & \sum_{k=1}^{p} \|\alpha^k\|_1 \\ \text{s.t.} \quad & \Phi_j[P(\{\Psi(\alpha^k)\}_{k=1}^{p})]_j = y_j, \ \forall j \in 1, ..., M. \end{aligned} \tag{4.2}$$

The optimization problem in Eq. (4.2) can be solved efficiently by an iteratively alternating minimization procedure. At iteration t of the algorithm, a noisy estimate G_t of the original image consistent with the observations is reconstructed based on the information from the previous iteration. The estimates of the coefficients $\{\alpha_t^k\}_{k=1}^{p}$ at this iteration can then be found by thresholding the coefficients of the noisy patches $\{x_t^k\}_{k=1}^{p}$ extracted from G_t.

Because we acquire compressive 1D pseudorandom line scans with a horizontal resolution set by the pulse spectral width and chirp processing parameters, the recovered vertical dimension N_v can be used as a tuning parameter depending on the complexity of the objects under test. In the reconstruction process, we use an effective M_l samples per line, far fewer than the number of pixels per line N_l where the full dimension $N = N_l \times N_v$. Thus, the compression ratio, line rate, and pixel rate are related to

the average number of samples needed to reconstruct each line in the image by

$$\text{Compression ratio} = \frac{M_l}{N_l}, \;\; \text{Line rate} = \frac{f_s}{M_l}, \;\; \text{and} \;\; \text{Pixel rate} = f_s \frac{N_l}{M_l}$$

where f_s is the pulse repetition rate and ADC sampling rate. Because the pixel rate of conventional systems is directly determined by the maximum usable ADC sampling rate, we refer to this primarily as the system figure of merit.

4.7 Experimental Results

4.7.1 Low Magnification

We construct a high-speed test image using laser-printed transparencies fixed to the platter of a dismantled 7200-RPM (rotations per minute) hard drive. The printed test objects are positioned on the outer edge of the spinning platter, measured to be moving at 34.3 m/s. The transparencies offer complex customized test objects with microscale features to measure the system performance at low magnification. Figure 4.4 depicts the raw voltage data acquired from two of the test objects. Each compressive measurement arrives as a scaled impulse response on the photodetector, which can be reduced to a single ADC value by synchronizing the ADC clock to the peaks of the pulses for maximally efficient sampling [102].

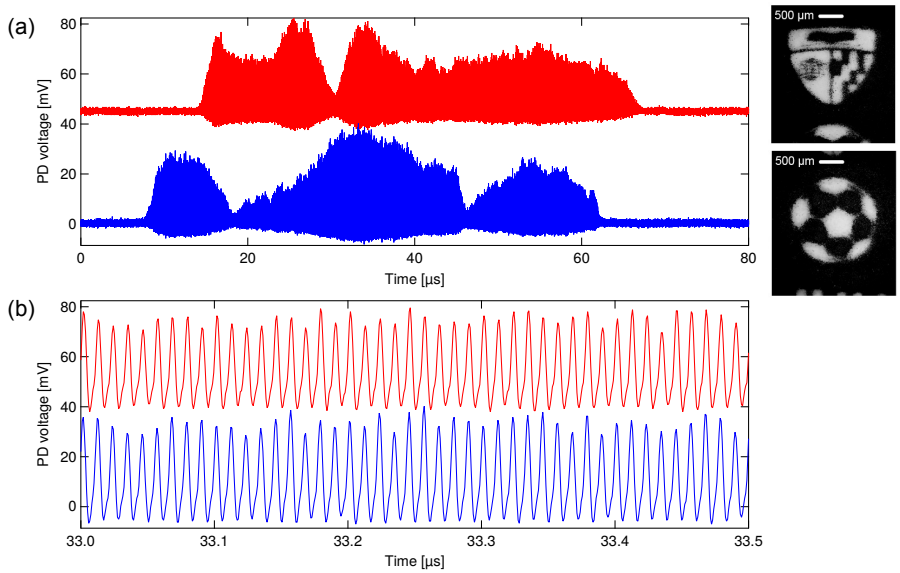

Figure 4.4: Raw experimental data from the low magnification CHiRP-CS system showing the recorded impulse responses of the detector at (a) coarse timescale and (b) fine timescale.

Our reconstructed results in Fig. 4.5 demonstrate imaging of complex objects moving at high speed from far fewer measurements than required in conventional Nyquist sampling. The first column shows optical microscope images of the static test objects for the purpose of comparison. Each subsequent column shows images of the objects moving at high speed taken with our compressive imager. Each of these images is reconstructed from 8400 consecutive measurements acquired in a single shot in 93.3 μs. Each column shows image reconstruction using a different relative percentage of measurements to recover the full image dimension. Therefore, the 6.15, 2.15, and 1.23% compression ratios in Fig. 4.5 correspond to imaging rates of 1.46, 4.19, and 7.32 Gigapixel/sec, which vastly exceed the present 90-MHz sampling rate.

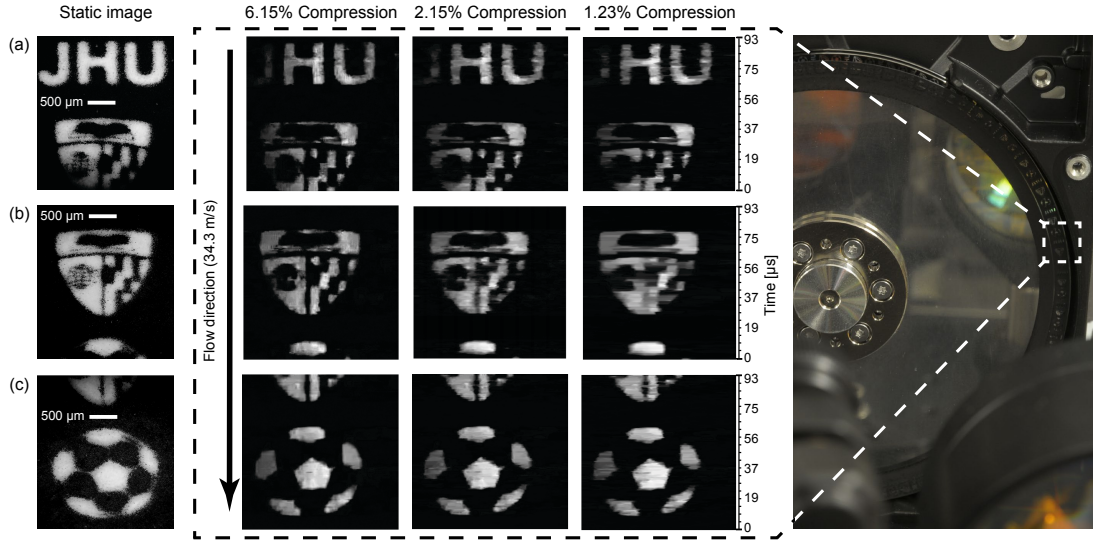

Figure 4.5: A laser-printed transparency with three objects of varying complexity (rows a–c) was fixed to the top platter of a 7200-RPM computer hard drive and imaged by the system at compression ratios of 6.15, 2.15, and 1.23%. The unevenness in the illumination is due to the spectral envelope (Fig. 4.2), which was left un-compensated in these results.

The compression ratio is practically limited by the complexity of the object's spatial features. For example, simpler objects such as the soccer ball in Fig. 4.5 in row (c) show very little loss of image quality as the compression ratio decreases whereas more complex objects such as the shield in row (b) become noticeably distorted in the horizontal dimension.

4.7.2 High Magnification

To demonstrate the CHiRP-CS system's potential for high-speed imaging of micron-scale objects (Fig. 4.1(e)) with correspondingly reduced signal contrast, we acquire images of a cluster of 25-µm undyed polystyrene microspheres dried onto

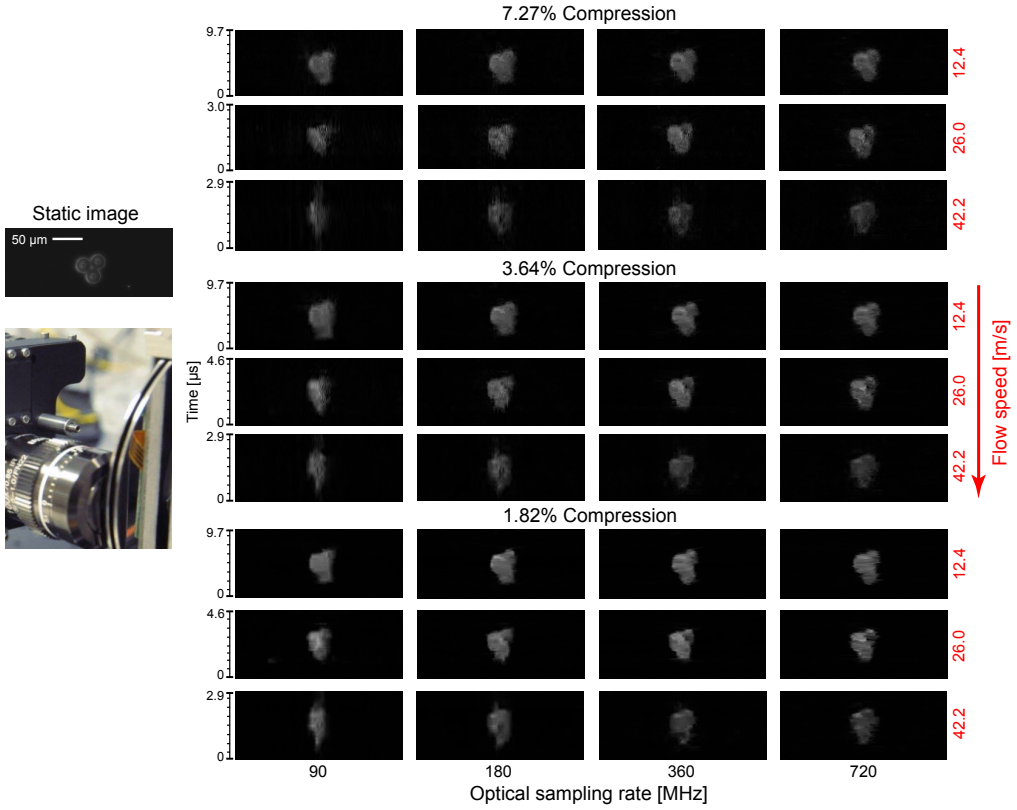

Figure 4.6: A single cluster of 25-µm undyed polystyrene microspheres imaged by the extended system, depicted in Fig. 4.1(c-e), moving at 12.4, 26.0, and 42.2 m/s using compression ratios of 7.27, 3.64, and 1.82%. The measurements were acquired at the interleaved pulse rate of 720 MHz and downsampled to the equivalent of 360, 180, and 90 MHz pulse rates for comparison.

the surface of the platter; the hard disk motor is now driven by a variable DC brushless motor controller. Figure 4.6 depicts reconstructions of the cluster moving at 12.4, 26.0, and 42.2 m/s from 7000, 3350, and 2140 measurements respectively at measurement rates from 90-MHz up to the interleaved 720-MHz using 7.27, 3.64, and 1.82% of Nyquist sampling. Note, each row of the figure corresponds to a single acquisition at 720 MHz and downsampled versions at 360, 180, and 90 MHz in order to demonstrate the benefit of the increased optical sampling rate for high-speed

flows. At 12.4 m/s, the shape of the microsphere cluster is well-represented at all sampling rates and compression ratios, but with some distortion at 90 MHz. There is also some characteristic horizontal blurring within the cluster at the higher compression ratio. At 42.2 m/s, though the reconstructed image contrast is reduced, the cluster shape shows excellent agreement in the 720 MHz case, but there is significant motion distortion that increases with lower sampling rate. At 1.82% compression, the loss of horizontal resolution at very low compression ratios prevents differentiation of the particles, but the overall size and shape of the cluster are well reconstructed. These results demonstrate image reconstruction of very high-speed microscopic flows at effective 9.9, 19.8 and 39.6 Gigapixel/sec rates from a maximum 720 MHz acquisition rate. To our knowledge these measurements are of the fastest flow rates to date for a diffraction limited microscopic line scan imager [82].

To reconstruct the microspheres as bright objects on a dark background, we acquire a reference trace on the ADC with no objects inside the field of view and compute a difference signal with objects in the field of view and input this into the reconstruction. The static image included for reference in Fig. 4.6 was acquired with a separate visible light microscope using dark field illumination. Thus, there is some uncertainty in how the interior regions of the microspheres should ideally appear under the system's near-IR confocal illumination.

4.8 Discussion

In addition to data compression, the compressive sampling technique presented here also results in considerable benefits for the signal to noise ratio of the measurements. On average, half of a pulse's spectral features are given a high '1' intensity level and half will be given a low '0' level. Thus the output pulse energy per sample is proportional to half of the unmodulated pulse energy. On the contrary, for conventional systems the energy per sample is inversely proportional to the total number of pixels. For example, in STEAM, considerable optical amplification (25–30 dB) is required to raise the optical signal above the detection noise floor [76, 79]. While the CHiRP-CS approach demonstrated here is entirely compatible with optical amplification of the output signal, it was not necessary for the results presented here.

The system presented here successfully extends CS imaging to continuous ultrahigh sampling rates. Compressive pseudorandom structured illumination reduces the required sampling bandwidth and information storage capacity by shifting signal processing complexity to the image reconstruction process. Thus, for the proposed high throughput flow cytometry application, online processing can be employed to exclude empty frames, but offline processing will be required to complete the image reconstruction and analysis, similar to commercial imaging flow cytometers [69]. The system offers a benefit nonetheless by increasing the achievable image acquisition speeds and by achieving real-time efficient image compression. More test samples can thus be analyzed by the imaging apparatus in less time with more efficient data

storage. Image post-analysis can be completed with inexpensive, readily available, and increasingly powerful computing hardware.

Compressive sampling opens a path to significantly higher speeds by increasing the information content gained per digital sample. For conventional Nyquist-sampling systems, the most efficient mode of operation is to acquire one sample per output image pixel. Typically, each image line is encoded on a single laser pulse and each pulse is sampled a number of times corresponding to the number of pixels per line. In contrast, we operate with a higher pulse repetition rate and each pulse is sampled once corresponding to a single compressive measurement. We demonstrate high-speed imaging using a smaller number of measurements corresponding to only a few percent of the total number of image pixels. In other words, at the same ADC sampling rate, this compressive system can perform 10–100× faster. In addition, because the system relies on structured illumination with straightforward single-pixel output photodetection, it can be readily adapted for imaging of fluorescence. Beyond imaging of flows, by employing a 2D spatial disperser [103], the system can be readily adapted to 3D compressive video measurements [104] of ultrahigh-speed phenomena. Furthermore, this all-optical approach to compressive measurements can increase dramatically the speed and efficiency of multiple optical measurement modalities, for example, real-time spectroscopy [105], swept-source optical coherence tomography [106], and high-speed microwave measurement [37, 50, 51].

Chapter 5

Spectral Shearing Contrast Quantitative Phase Microscopy

Photonic time-stretch microscopy enables record-high throughput imaging for bioparticle classification in flows. While several demonstrations have adapted quantitative phase techniques to time-stretch microscopy, they have relied almost exclusively on sensitive free-space interferometers and spatial filters. In this chapter, we present a straightforward high-performance technique using self-referencing of ultrashort pulses in a fiber spectral shearing interferometer to measure the amplitude and phase images of low contrast microscopic subjects at very high speed. We demonstrate quantitative phase imaging up to 400,000 cells/second.

5.1 Label-Free Time-Stretch Microscopy

As discussed in section 4.1 and 4.2, imaging flow cytometry (IFC) is a recent improvement to traditional flow cytometry (FC) for single-cell characterization and sorting of very large heterogeneous populations up to millions of cells. FC is widely used throughout basic cell and molecular biology, genetics, immunology, and environmental science to quantify the phenotypes and physiological responses of individual cells [63, 64]. IFC supplements the single-pixel scattering and fluorescence measurements of traditional FC with 2D images, significantly increasing the amount of information gained from each particle by resolving two-dimensional brightfield and fluorescent images of the particles in flow. However, to avoid motion blurring, IFC supports flows only up to several cm/s, limiting the analysis rates to ∼1000 particles/s [69,70].

Photonic time-stretch microscopy (TSM), which utilizes dispersive frequency-to-time mapping in optical fiber [107] to read out image pixel information serially with a single photodiode (PD) and analog-to-digital converter (ADC) [79, 80, 108], has been demonstrated to be an excellent solution for high-speed observation of particles in microfluidic flows [76]. Under TSM, each pulse of a mode-locked laser (MLL) represents a single line or frame, permitting ∼ps exposures and 10-1000 MHz exposure rates. Identifying rare cells from a sample of biofluid is a compelling application of time-stretch flow microscopy because its inherent capability for high speed can reduce by several orders of magnitude the time necessary to analyze a sample and detect events with exceedingly low incidence (e.g., below 1 ppm).

CHAPTER 5. SPECTRAL SHEARING CONTRAST QUANTITATIVE PHASE MICROSCOPY

With the problem of high-speed efficient acquisition addressed, one must address the image contrast mechanisms available for characterizing the cells. High-throughput particle classification in biofluids has traditionally relied on one or several biomarkers to identify cells of interest. However, this approach always suffers from the problem of cell-labeling specificity: the ratio of correctly labeled particles to nonspecific background ultimately determines the signal-to-noise ratio (SNR) of the measurement more than the SNR of the instrument [66]. The general problem of signal-to-noise in cell labeling specificity and the corresponding need for excellent sample preparation makes label-free imaging a very attractive possibility for cell classification.

Thus, several works have recently attempted to improve the achievable image contrast of unlabeled cells in suspension under TSM. Classical differential interference contrast (DIC) using a Nomarski prism has been implemented on a TSM system [109], permitting improved image contrast by mapping phase gradients to intensity. By adding a beamsplitter to create a reference arm with a second identical objective and reference mirror such that the sample sits in one arm of a Michelson interferometer, it is possible to detect spectral interference fringes that can then be used to unwrap the spatial phase shift due to the sample [81, 110, 111]. Common-path designs have also been proposed [112]. In this way, it was possible to classify cells based on diameter and refractive index contrast, used as a measure of protein concentration. More recently, a technique called asymmetric-detection time-stretch optical microscopy (ATOM) for label-free image contrast enhancement was devel-

oped that relies on asymmetric coupling of the light from the sample into the optical fiber preceding amplification and readout [82]. In this technique, the light returned from the sample is split into two paths (one is delayed relative to the other in order to create temporally multiplexed linescans) and the two arms are focused into the same optical fiber but on opposing small angles θ relative to the optical axis of the fiber and input collimating lens. The off-axis coupling effectively blocks part of the cone of light received from each point on the object (recall that the end of the fiber core is confocal with the points in the sample and the sample points are separated spatially according to wavelength) without the additional requirement of coherent interference. The contrast mechanism is more-or-less equivalent to differential phase contrast (DPC) microscopy [113] and Schlieren photography. The use of multiple arms allows for computation in post-processing of a differential image with further enhanced contrast; to acquire quantitative phase images, the system was extended to four asymmetric collection fibers, time-multiplexed for readout at the ADC [114].

5.2 Experimental System

Here, we adapt a technique from single-shot ultrashort pulse characterization for amplitude and phase observation of low-contrast samples under TSM by using spectral shearing interferometry. The technique affords simplicity, robustness, and tunability while achieving performance that equals the state of the art.

The system (Fig. 5.1) consists of a high magnification spectrally-mapped linescan microscope, spectral shearing Sagnac loop interferometer, and dispersive frequency-to-time mapping and serial readout in succession. Inside the microscope, a 600 line/mm diffraction grating and 175-mm focal length Fourier transform (FT) lens map the spectrum of 300-fs ultrafast mode-locked laser (MLL) pulses onto a one-dimensional (1D) line at the image plane of a 60× NA = 0.7 polarized light microscope objective and f = 175 mm tube lens system. To operate the microscope in transmission mode, a second 50× NA = 0.8 objective and tube lens are used to focus the line image onto a mirror. A microfluidic device placed between the objectives carries a laminar flow of particles moving up to several m/s for high-throughput observation. Light double-passed through the flow is spectrally recombined and collected back into the input fiber and directed with an optical circulator into the spectral shearing interferometer. The interferometer splits the pulse into sheared and unsheared copies that are delayed relative to each other to create the spectral interference fringes for detecting the spectral amplitude and phase of each pulse after dispersive frequency-to-time mapping, photodetection, and digitization. As objects move through the system field of view at a constant velocity, 2D images are acquired with a vertical dimension that corresponds to both time and vertical spatial extent.

Spectral shearing is achieved with a 20-GHz $LiNbO_3$ electro-optic phase modulator (ϕM) driven by an 11.52-Gbit/s pulse pattern generator (PPG) synchronized to the MLL. The PPG and RF bandpass filter are employed to generate a sinusoidal tone

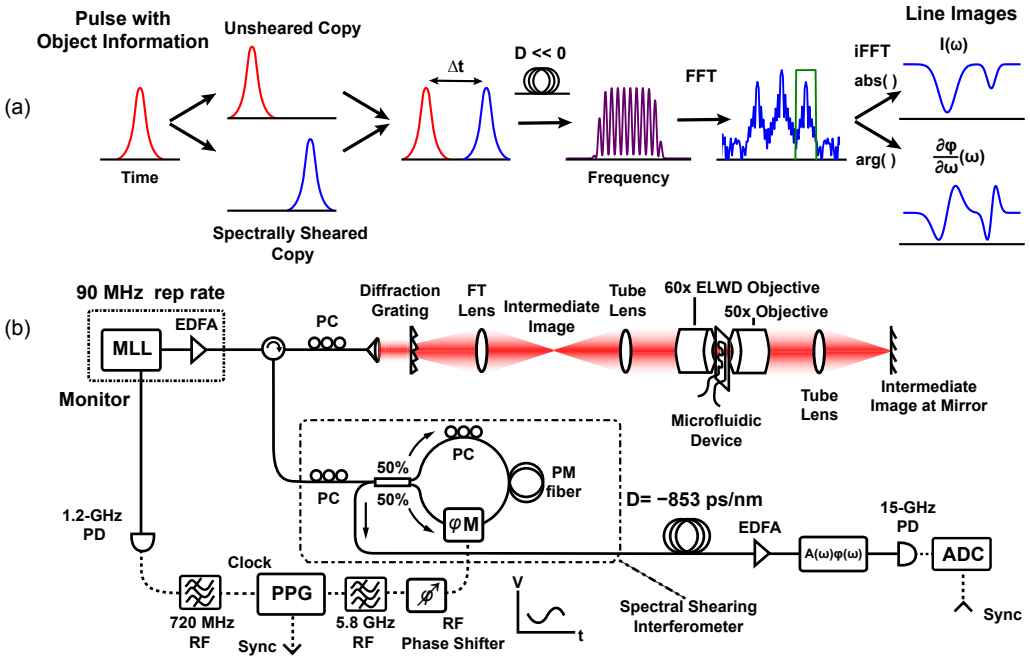

Figure 5.1: (a) Conceptual operation: The spectra of broadband MLL pulses are imprinted with an object's amplitude and phase information. Each pulse is split into two copies (one of which is spectrally sheared) and recombined with a relative time delay. The spectral interference is read-out via dispersive frequency-to-time mapping. Finally, the intensity and differential phase line images are read out by filtering the FFT of each pulse spectrum. (b) System schematic in detail.

at $f = 5.76$ GHz (64^{th} harmonic of the 90 MHz MLL repetition rate). The optical pulse train returning from the microscope is synchronized to the zero crossings of the RF waveform by optimizing the RF phase shifter. Under this condition, the driving voltage $V(t) = (\pi V_p/V_\pi)\sin(2\pi f t)$ produces a sheared field $E(\omega - \Omega)$ where $\Omega = 2\pi^2 f V_p/V_\pi$ [115, 116]. For the phase modulator and RF amplifier employed here, a shear up to Ω=116 GHz (0.15 nm) is readily achieved. Because the shear Ω can be controlled electronically by the amplitude or frequency of the RF voltage $V(t)$, the "contrast" can be easily adjusted to image large or small object phase gradients.

Inside the fiber interferometer (dashed outline in Fig. 5.1), the counterclockwise propagating pulse travels in the correct polarization state and direction for the electro-optic phase modulator (ϕM), thus it experiences a spectral shear. After traveling through an additional 8 m of polarization-maintaining (PM) fiber, a fiber polarization controller (PC) acts as a half-lambda plate to rotate the polarization by 90 degrees. The clockwise propagating pulse undergoes this polarization rotation first and then travels through the PM fiber and ϕM in the orthogonal polarization state, experiencing a different polarization mode delay in the loop compared to the counterclockwise pulse. Because the clockwise pulse also travels through the ϕM in the wrong polarization state and direction for phase modulation, it remains unsheared. At the output of the loop, a sheared and an unsheared pulse, time-delayed relative to each other, emerge rotated 90 degrees from the input polarization state [116]. We have previously demonstrated a proof of concept version of this imaging system [117] that relied on an asymmetric Mach-Zehnder fiber interferometer with the phase modulator in one arm and a tunable delay in the other (and PCs in both to set the polarization states). The Sagnac loop has proven in our experiments to be extremely stable in comparison to the previous fiber Mach-Zehnder interferometer. The linear phase $\tau\omega$ of the spectral interference fringes barely shifts over the course of an half-hour in our studies without any thermal stabilization, permitting longer integration times over several pulses for higher sensitivity measurements.

The Sagnac loop's advantage in stability also appears in comparison to a free space interferometer: in [111] a standard grating-based optical spectrum analyzer (OSA) introduced considerable noise compared to time-stretch readout due to its longer integration time. Here the improved stability permits integration times far longer than the order of seconds for an OSA sweep. Other sources of mismatch such as the interferometer pulses' polarization state and power [81,111], affecting the signal to background ratio of the interference fringes, are mitigated in this approach.

The dispersive frequency-to-time mapping is performed in a normal dispersion fiber (DCF) with $D = -853$ ps/nm. A C-band erbium-doped fiber preamplifier compensates the loss in the microscope and dispersing fiber. A programmable amplitude and phase spectral filter (SF) immediately preceding the photodetector and ADC serves both to flatten the optical spectrum, effectively creating uniform received illlumination power over the full field of view, and to compensate the third order dispersion (TOD) in the DCF, which would typically contribute an erroneous quadratic component to the measured phase after the $\partial\omega/\partial t = (\beta_2 L)^{-1}$ frequency-to-time mapping where L is the length of the dispersing fiber. In addition, the SF is used to set an output optical bandwidth of 1.5 THz that prevents overlap between time-stretched pulses at the 90 MHz MLL repetition rate. The polarization mode dispersion introduced by the ϕM and the PM fiber inside interferometer creates a delay of 36.5 ps between the sheared and unsheared pulses. This results in a center frequency of 5.32 GHz in the FFT of the interference signal after time-stretching.

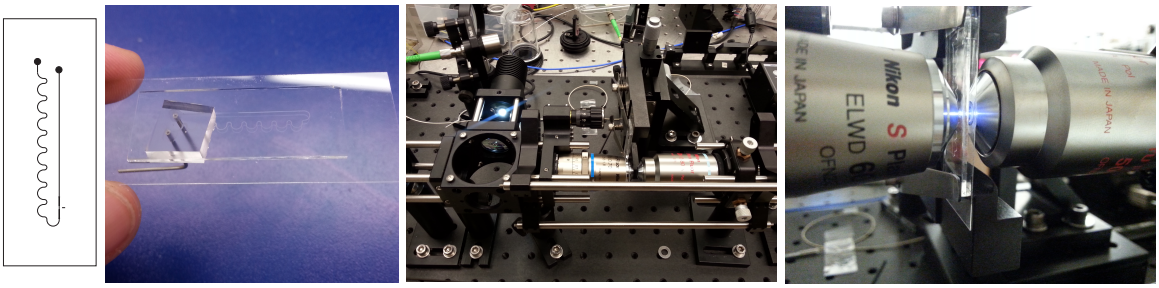

Figure 5.2: (a) Microfluidic CAD design for photolithography. Photographs of a finished device (b) and (c–d) a test device in the optical path without fluid inlets.

The spectrally sheared and time-delayed (by time τ) copies of the field $E(\omega) = \sqrt{I(\omega)}\exp(\phi(\omega))$ returned from the object yield a measured spectrum $S(\omega)$ with an interferometric argument $\Delta\phi = \phi(\omega) - \phi(\omega - \Omega) - \tau\omega$ that permits direct measurement of the finite difference of $\phi(\omega)$ retrieved by bandpass filtering the Fourier transform of $S(\omega)$. This fact is analogous to traditional DIC imaging wherein two polarization components are laterally sheared by a Nomarski or Wollaston prism and then recombined, permitting the output amplitude to represent small spatial derivatives in the optical path length. Here, the small spatial derivative in the object phase is read out from the interference fringe phase. The raw differential phase images have a characteristic appearance as if illuminated from the side.

The microfluidic channel has a 140 μm wide by 40 μm tall rectangular cross section (see Fig. 5.3) with asymmetric curving segments for inertial focusing of the particles into the center of the channel cross section [76, 81, 82, 118] prior to a tapered region with 50 μm width at the observation line. It is fabricated in Polydimethylsiloxane (PDMS) using soft lithography and bonded via plasma oxidation to a glass

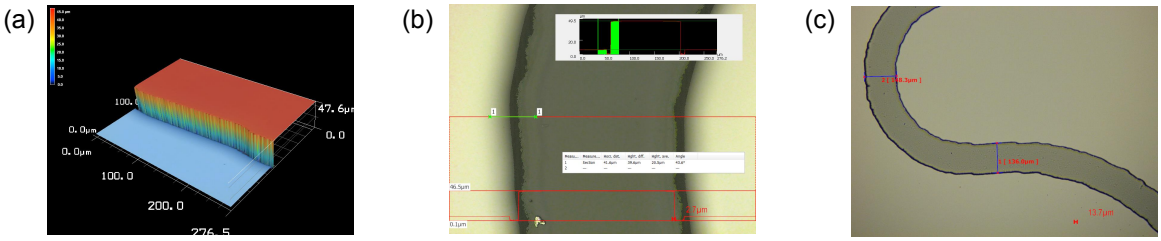

Figure 5.3: 3D profilometer measurements of the SU-8 photoresist on silicon master for making the microfluidic channels. Highlighted are the (a) 3D profile of one sidewall, (b) channel height, and (c) channel width measured at two points along the length. Roughness is due to the resolution of the printed photolithography mask.

coverslip following standard protocols [119]. To facilitate high magnification imaging through the channel, the PDMS slab thickness is set to 1 mm except at the inlets where an additional 3 mm slab of PDMS is bonded to stabilize the tubing connections. The glass correction collar on the 60× objective (Nikon CFI S Plan Fluor ELWD) is optimized for observation through the PDMS and the 50× objective (Nikon TU Plan Fluor) observes through the coverglass. Additional discussion of the microfluidic system can be found in section 6.2.2.

5.3 Experimental Results

Figure 5.4 depicts the system's capability for high throughput flow imaging of cells. A sample of marine phytoplankton (genera Nannochloropsis and Chlorella) were flowed through the channel at 5 m/s average velocity. The intensity and differential phase images from a buffer of 256 MSamples acquired in real time at 40 GSample/s (corresponding to 6.4 ms duration) is depicted on the left. In the middle are the

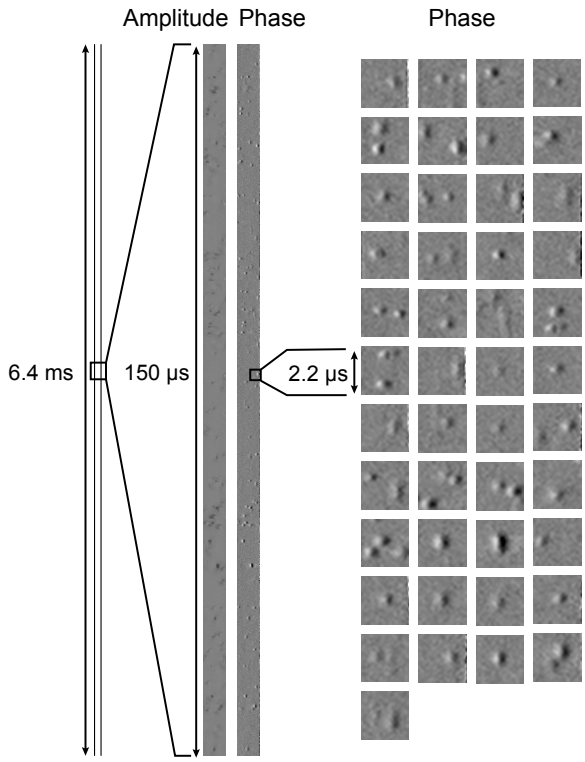

Figure 5.4: High-throughput imaging of phytoplankton flowing at 5 m/s. Intensity and differential phase images from a 256 MSample single-shot acquisition, 6.4 ms in duration, are depicted in full (left) and zoomed in to 150 µs (middle). Segments (right) of the differential phase images containing individual particles and small clusters are automatically selected in software.

intensity and differential phase images from 150 µs of this acquisition. On the right are segments of the differential phase image centered on individual particles and small clusters, selected automatically in software via thresholding for positive and negative polarity features in the differential phase image. Thus, we demonstrate single particle analysis at a sustained rate of 400,000 cells/s.

Figure 5.5 depicts experimental results with reference objects: baker's yeast (Saccharomyces cerevisiae) and red blood cells in whole blood. Samples were placed under a cover slip and stepped through the system field of view in steps of 250 nm for

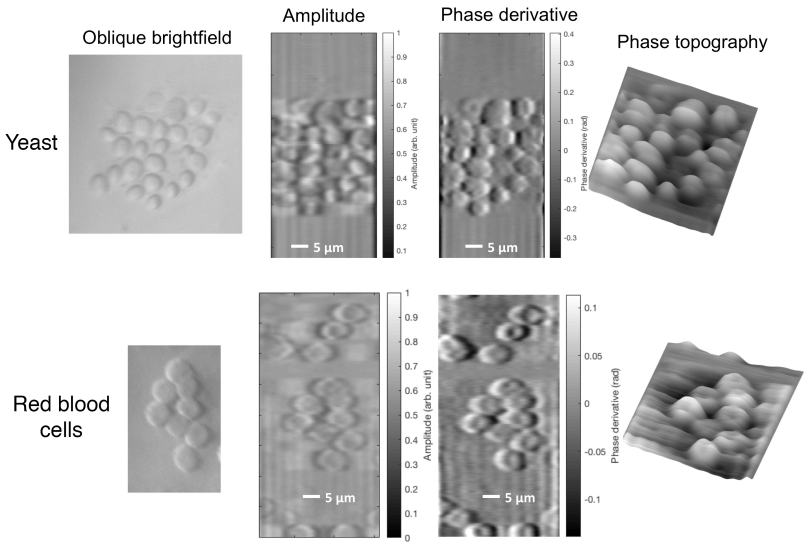

Figure 5.5: Experimental results with reference objects: low contrast yeast and red blood cells.

comparison with conventional imaging using a CMOS sensor. In the left column are conventional images under the system's microscope (utilizing a dichroic mirror, white LED source, and sensor not pictured in Fig. 5.1) using oblique brightfield illumination for improved contrast. In the middle two columns are the raw amplitude and differential phase images returned from filtering the FFT of the interference fringes. On the right are 3D plots of the phase obtained by numerical integration of the differential phase images across the frame, taking into account the shear distance Ω, which is the only calibration necessary for accurate quantitative phase measurements.

The measured complex field $E(\omega)$ also provides a unique benefit in terms of computational refocusing after the image acquisition. Ideally, hydrodynamic focusing can localize all of the particles within the system field of view and depth of field (DOF). However, inertial focusing requires matching of the flow velocity and the

particle size [118], allowing many particles in a heterogeneous mixture not to meet the focusing criterion. The ability to refocus the high magnification (i.e. shallow DOF) images permits many more usable frames to be derived from nonideal flow conditions. To refocus the images, we compute the field $E_{out}(x,z)$ resulting from 1D scalar diffraction of the line images $E_{in}(x)$ (x replaces ω to represent the wavelength to space mapping in the microscope) using the angular spectrum (AS) method approximation to the Rayleigh-Sommerfeld integral:

$$\tilde{E}_{in}(k_x) = F\{E_{in}(x)\} = \int E_{in}(x)\exp(-jk_x x)dx$$

$$G(k_x,z) = \exp(jz\sqrt{k_0^2 - k_x^2})$$

$$E_{out}(x,z) = F^{-1}\{\tilde{E}_{in}(k_x)G(k_x,z)\}$$

$$E_{out}(x,z) = \frac{1}{4\pi^2}\int \tilde{E}_{in}(k_x)G(k_x,z)\exp(jk_x x)dk_x$$

where $F\{\cdot\}$ and $F^{-1}\{\cdot\}$ denote the forward and inverse Fourier transform (i.e. FFT) and $G(k_x,z)$ is the 1D optical transfer function in the spatial frequency domain [120]. As before, the 2D image is formed by stacking the refocused 1D line images. Figure 5.6 demonstrates refocusing of a slightly out-of-focus image of baker's yeast in flow. The measured $I(x)$ and $\phi(x)$ images form the input field $E_{in}(x) = \sqrt{I(x)}\phi(x)$, which is diffracted through a path of several microns around the original focus of the microscope objective. In this case, refocusing the image by $z = -1$ μm leads to a better focus on the yeast cell in the lower right portion of the image.

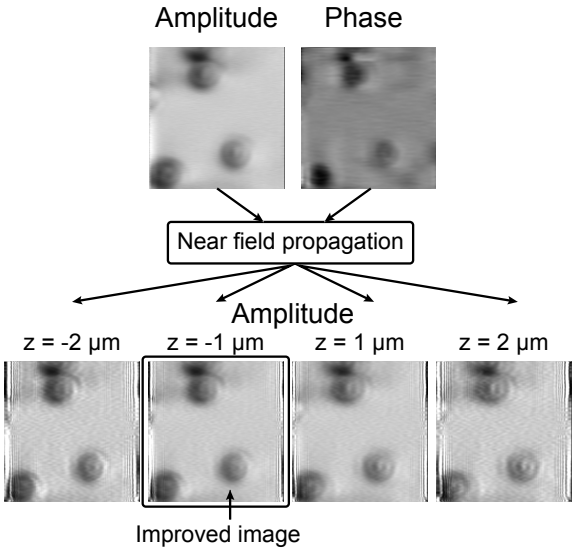

Figure 5.6: Computational refocusing after acquisition by applying 1D scalar diffraction (AS method) to the measured complex field, amplitude and phase (integrated from the differential phase image).

5.4 Discussion

In conclusion, we have demonstrated a new technique for acquiring quantitative phase images at a 90 MHz line rate using electro-optic spectral shearing and self-referencing of ultrashort MLL pulses. The self-referencing interferometer is extremely stable and free of alignment so it can be added to any spectrally mapped microscope. The technique directly yields intensity and differential phase images that are well suited to high-throughput classification of low contrast unlabeled cells in a microfludic flow. In this paper, flows up to 5 m/s and sustained cell imaging up to 400,000 cells/s were demonstrated. The measured complex field is also demonstrated to be refocusable for increased post-processing flexibility.

CHAPTER 5. SPECTRAL SHEARING CONTRAST QUANTITATIVE PHASE MICROSCOPY

Electro-optic phase modulators are readily available at $\lambda = 800$ nm and 1 μm and the technique can be readily extended to microscopy at these wavelengths. This should be the subject of future work.

Chapter 6

Ongoing Work

6.1 Multiplexed Detection Quantitative Phase Time-Stretch Microscopy

We present in this section a straightforward technique for multiplexing interferometric signals as a means to improve the SNR and electronic bandwidth of quantitative phase time-stretch microscopy, enabling better sampling rates and detection efficiency.

6.1.1 Introduction

The problem of high information content classification of very large numbers of particles in a biofluid has led to significant interest in label-free high-throughput

microscopy. In particular, photonic time-stretch microscopy (TSM), discussed in sections 4.2 and 5.1, has shown much promise for high-throughput observation of microfluidic flows [76]. Compared to other automated microscopes and imaging flow cytometers, TSM can reduce by several orders of magnitude the time necessary to analyze a sample and detect events with exceedingly low incidence (e.g., below 1 ppm). Because detection based on one or several biomarkers to identify cells of interest always suffers from the problem of cell-labeling specificity [66], several works have incorporated intensity and phase measurements via interferometry [81, 111, 112, 117] or differential phase contrast [82, 114].

Here, we extend quantitative phase TSM by capturing both outputs from the interferometer into a single fiber using polarization multiplexing to measure a differential interference signal that enables higher SNR detection and more efficient use of the digitization bandwidth.

6.1.2 Experimental System

The system (Fig. 6.1(a)) consists of a high magnification spectrally-mapped interferometric linescan microscope, polarization multiplexing step, dispersive frequency-to-time mapping, and polarization demultiplexing and photodetection in succession. Inside the microscope, a 600 line/mm diffraction grating and 175-mm focal length Fourier transform (FT) lens map the spectrum of 300-fs ultrafast mode-locked laser (MLL) pulses onto a one-dimensional (1D) line at the image plane of a 60× NA=0.7

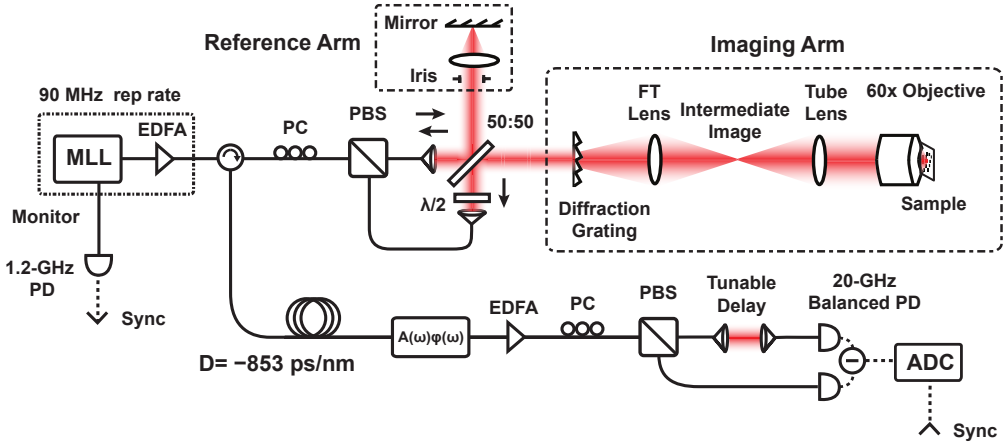

Figure 6.1: System diagram: the spectra of broadband MLL pulses are imprinted with an object's amplitude and phase information and these images are recovered via filtering of the FFT.

polarized light microscope objective and 175-mm tube lens system. As objects move through the system field of view at a constant velocity, 2D images are acquired with a vertical dimension that corresponds to both time and vertical spatial extent.

A polarization controller (PC) and inline fiber polarization beamsplitter/combiner (PBS) precede the collimated input to the microscope such that only horizontally polarized light enters. Inside the microscope, a 50:50 beamsplitter splits the input into an imaging arm (containing the grating, lenses, and objective) and a reference arm containing a lens and mirror on a 1-D linear stage. Light returned from the sample is collected back through the imaging arm such that the microscope acts as an asymmetric Michelson interferometer. After the imaging and reference arms recombine at the beamsplitter, one output path travels back into the input fiber and the second passes through a $\lambda/2$ waveplate (rotating the polarization by 90 degrees)

through a second collimator into the orthogonal polarization state of the PBS. In this way, both interference signals from the beamsplitter can be captured into a single fiber. After this polarization multiplexing, the returned light containing the image information is directed with an optical circulator into the dispersing fiber.

Dispersive frequency-to-time mapping is performed in a normal dispersion fiber (DCF) with $D = -853$ ps/nm. A programmable amplitude and phase spectral filter (SF) preceding the erbium-doped fiber amplifier (EDFA) acts a bandpass filter; it can also be used to flatten the optical spectrum to create uniform received illumination power over the full field of view (FOV) and to compensate the third order dispersion (TOD) in the DCF. After amplification, the two polarization signals are demultiplexed with a second PC and PBS and matched in time and optical power into a highly-linear balanced 20-GHz photodiode. Between the mux and demux stages, both signals travel in the same fiber and EDFA, making the system easier to assemble and more robust against noise and nonlinearity than could be achieved, e.g., by amplifying and then passing in opposing directions through the DCF before photodetection.

The time-delayed (by time τ) reference and image fields of the form $E(\omega) = \sqrt{I(\omega)}\exp(\phi(\omega))$ yield a measured spectrum $S(\omega)$ with a DC image component $I_{image}(\omega) + I_{ref}(\omega)$ and an interferometric component with the argument $\Delta\phi = \phi_{image}(\omega) - \phi_{ref}(\omega) - \tau\omega$ that can be retrieved directly by bandpass filtering the Fourier transform of $S(\omega)$. Because the beamsplitter produces two outputs with a π

phase difference in the interference term, both can be used in a differential manner to cancel the DC component and double the power in the interferometric component.

6.1.3 Results

A challenge for interferometric TSM using a single-ended photodetector is the high sampling rate required to capture an interference fringe mapped to a high-frequency temporal signal. Previous works have chosen center frequencies of 5 GHz or more to prevent aliasing between the image information centered at DC and the interference terms. Here, we effectively cancel the image information centered at DC, permitting more efficient use of the ADC sampling bandwidth. Assuming similar bandwidth between the DC and interference terms, the single-ended measurement requires 50% more electronic sampling bandwidth than the approach presented here. To demonstrate the intended benefit, we set the image-reference relative time delay in the microscope to lower the interference fringe to 2 GHz (digitized at 10 GSample/s) and compare the single-ended and differential measurement cases.

In Fig. 6.2, time-stretched interference fringes are depicted for the differential system presented in Fig. 6.1 and the same system with one arm blocked at the demultiplexing PBS. The cancellation of the unused DC image appears excellent: the central peak on the FFT descends by more than 40 dB, touching the noise floor, and the interference peaks increase in power by the desired

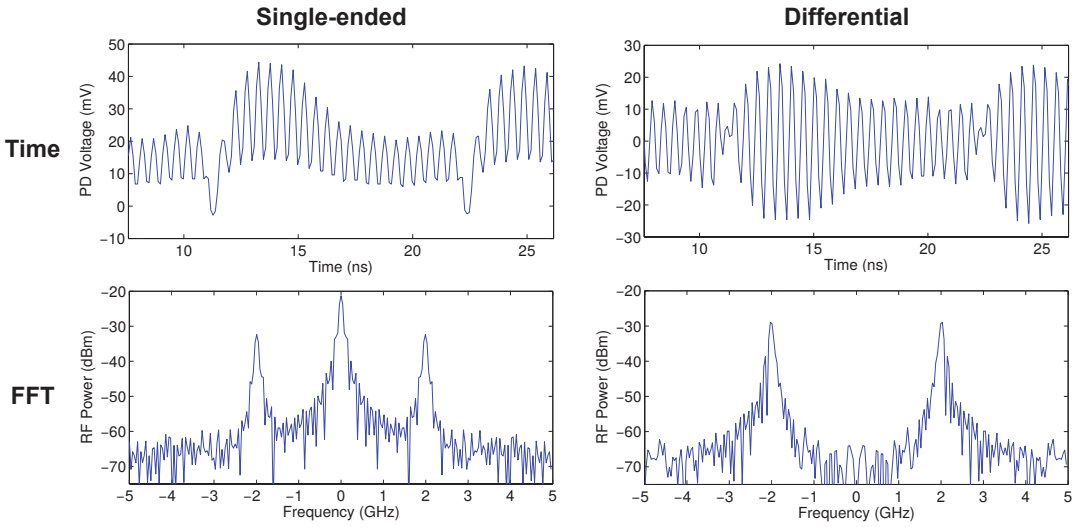

Figure 6.2: A single-ended and full differential measurement (showing full cancellation of the unused DC image) are compared in time and frequency.

3 dB. Thus, the reasonable width of the bandpass filter in post-processing can be much broader to increase the system resolution.

To test imaging of the intensity and phase of a low contrast subject, a sample of baker's yeast (Saccharomyces cerevisiae) in water was stepped through the microscope field of view in increments of 250 nm and a single-shot measurement of one pulse was collected at each step (Fig. 6.3). The filter bandwidth for recovering the intensity and phase images was centered at 2 GHz with a 1.9 GHz half-width. The images from the differential measurement achieve essentially the full resolution available to the ADC without aliasing, while the single-ended measurement experiences tremendous distortion in trying to achieve the same resolution and bandwidth efficiency.

To demonstrate the system's potential for high throughput, a larger sample of yeast cells was prepared and moved at maximum rate through the FOV on a servo

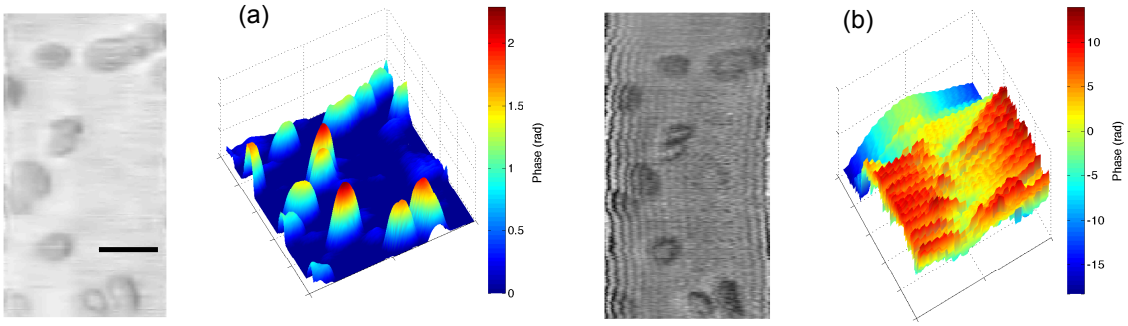

Figure 6.3: Reconstructed intensity and phase images of a sample of yeast cells using the full ADC sampling bandwidth. (a) The differential measurement system produces accurate images with the maximum resolution (i.e., filter bandwidth). (b) The single-ended measurement experiences significant aliasing with the wide filter bandwidth producing artifacts in the intensity image and a completely unusable phase image. Scale bar: 10 μm.

stage. The yeast appear with much better contrast in the phase images (located on the right in each pair) and the overlapping of cells is much more apparent than in the amplitude images (located on the left in each pair). By calculating the standard deviation across localized regions of the phase images, we estimate the phase noise to be $\sigma = 0.011$ rad, which is comparable to the state of the art for TSM [110].

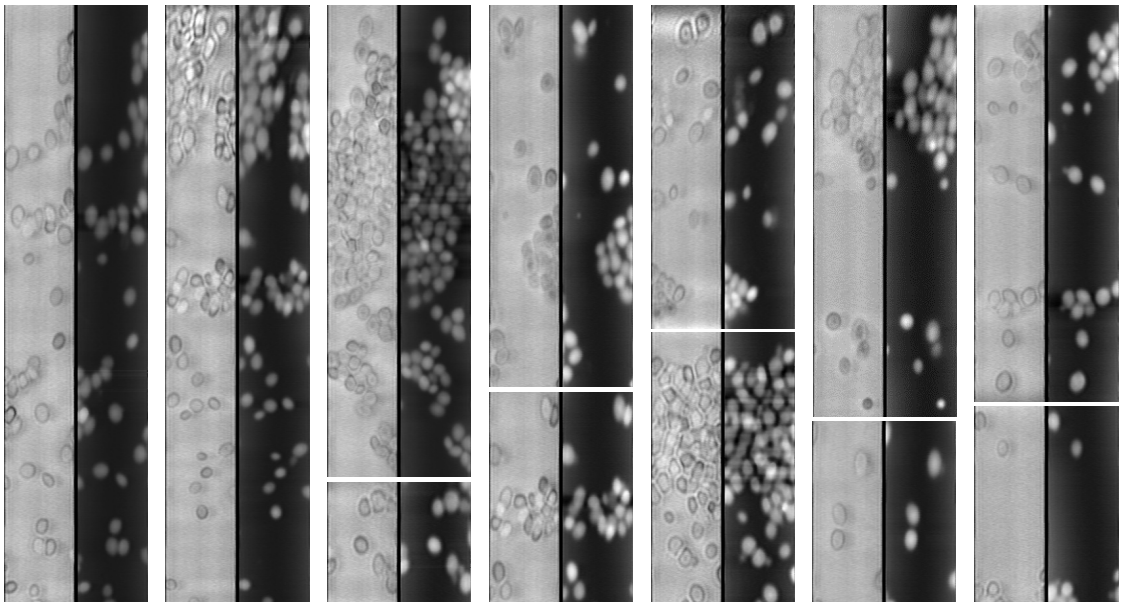

Figure 6.4: Larger scale measurement of yeast on a moving slide. The paired images are amplitude on the left and phase on the right.

6.2 Diffraction Interference Time-Stretch Microscopy

6.2.1 Optical System

The double-pass transmission microscope depicted in Fig. 5.1 provides a straightforward means to illuminate the sample and collect the returned light through a single fiber, diffraction grating, and Fourier transform (FT) and tube lens pair. The second objective (50×) and tube lens permit accurate positioning of the center of the microfluidic channel into the center of the system field of view (FOV) and depth of field (DOF). The alternative is to use only one objective and bond the microflu-

idic channel to a mirror or glass substrate with gold deposited below the observation area of the channel [76, 81]. Using a mirror permits simple alignment, but makes it difficult to focus particles within the DOF of the microscope. Moreover, it significantly increases the cost of each microfluidic channel (PDMS and glass coverslips are much more affordable by comparison), which often should be treated as single-use devices in order to prevent cross-contamination.

The downside to the double-pass configuration is the attenuation incurred in the microscope objectives: each pass through the pair of objectives causes close to 6 dB loss. There is also a presumed loss of resolution due to the repeated effect of the lens modulation transfer functions (MTF).

Thus, a new single-pass configuration was developed that would bring several advantages (Fig. 6.5). The FT and tube lenses from chapter 4 through here form a Keplerian telescope that creates angular magnification (M) before (or after) the microscope objective. The pair of infinite conjugate microscope objectives can also be viewed as a telescope with a focal length ratio $f_{\mathrm{M1}} = 3.33$ mm : $f_{\mathrm{M2}} = 4$ mm due to the 60× and 50× magnifications with intended $f = 200$ mm tube lens. Viewing the system as a chain of three telescopes, it is necessary to return the total magnification to unity so that the beam divergence matches the input and the wavelengths can be recombined successfully for efficient coupling into the output fiber. To this end, the magnification of the third telescope must take into account the different focal lengths of the microscope objectives and take on a 6:10 focal length ratio rather than 5:10. (The grating

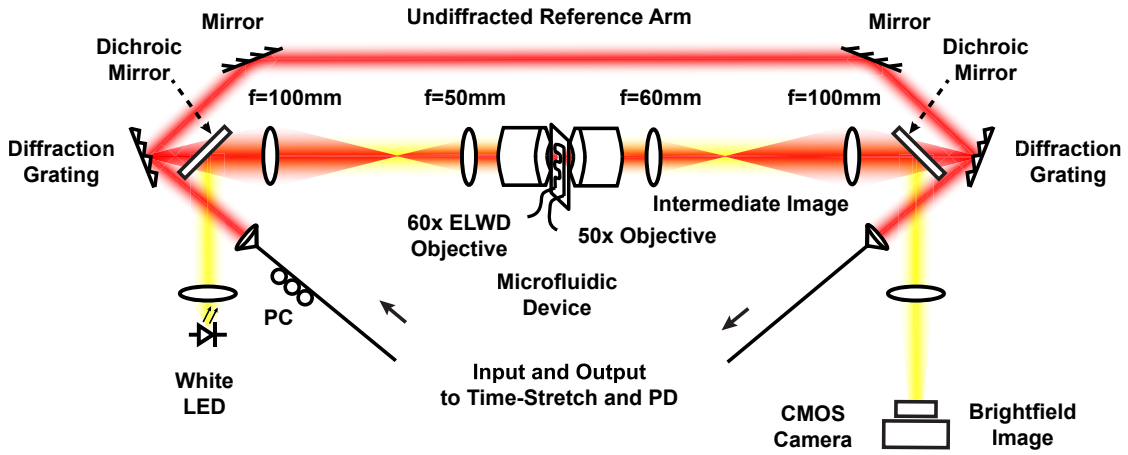

Figure 6.5: Schematic diagram of the diffraction interference microscope depicting the imaging arm, undiffracted reference arm, and white-light imaging paths.

angles must also be symmetrical to match the angular dispersion and beam ellipticity.) With these considerations, the loss in the aligned system is very acceptable: <6 dB coupling loss using packaged FC/PC collimators (Thorlabs, $f = 37.52$ mm).

The FOV can be calculated from these focal lengths along with the input magnification and the angular dispersion ($\frac{d\theta_{\mathrm{D}}}{d\lambda}$) of the diffraction grating

$$\mathrm{FOV} = f_{\mathrm{M1}} M \Delta\lambda \frac{d\theta_{\mathrm{D}}}{d\lambda} \tag{6.1}$$

where $\Delta\lambda$ is the optical bandwidth in use. The 1.46 nm/mrad dispersion of the 600 line/mm diffraction grating and the 100 mm : 50 mm lens ratio with $\Delta\lambda = 12$ nm sets the FOV = 55 μm. The new FOV is twice that presented in Fig. 5.1 and 6.1, suitable for larger mammalian cells in future investigations.

The second major advantage of the new design is that the Michelson interferometer can be abandoned by routing the undiffracted light (order $m = 0$) from the diffraction gratings to act like a Mach-Zehnder interferometer but with no beamsplitters! The relatively small amount of light that is undiffracted from the gratings matches quite well the loss in the microscope arm and the ratio can be fine-tuned elegantly by changing the input polarization to favor the grating's more efficient perpendicular (to the grooves) or less efficient parallel polarization state. The signal and reference paths are nearly common-path so the design is quite stable for a free-space interferometer.

The final advantage of the new microscope is that the linear layout permits simple addition of two dichroic mirrors for simultaneous visible imaging and perhaps fluorescence measurement for classification. The previous designs were set up only for intermittent white-light imaging (not simultaneous with normal system operation) by dropping in a visible beamsplitter into a 30 mm cage cube visible in Fig. 5.2(b) to form an epi-illuminated brightfield image using a dichroic positioned between the intermediate image and the tube lens.

6.2.2 Microfluidic System

As described in section 5.2, prior experiments utilized a microfluidic channel that relied on inertial focusing [118] of microparticles. In order to improve the robustness of focusing (i.e., decrease its dependence on particle size and fluid velocty) and si-

multaneously decrease the fluidic resistance in the channel, we've begun developing a 'Y'-junction channel to use a sheath fluid to provide hydrodynamic focusing.

We modify and expand on the model presented in [121]. Three 100 μm wide by 50 μm tall channels converge to one: the center carries the solution of cells or particles, the other two are angled at 60 deg to the center and carry a buffer fluid. Focusing can be customized by changing the ratio of the center (v_c) and left/right (v_{lr}) flow velocities. For example, in [121] it was experimentally demonstrated that a solution of fluorescein in a 200 μm channel could be focused to a width of 7.95 μm by setting the velocity ratio without dependence on the flow velocities.

In Fig. 6.6, we verify in a Comsol 5.2 simulation ($v_c = 1\mu$L/s and $v_{lr} = 2$ μL/s depicted) that the desired focusing takes place in a 3D laminar flow both for the transport of diluted species (Fig. 6.6(a)) and particle tracing in the presence of drag (Fig. 6.6(b-c)) models. Fabricating the devices and considering the morphological impact of forces experienced by cells inside the channel [122–124] will be the next subject of future work.

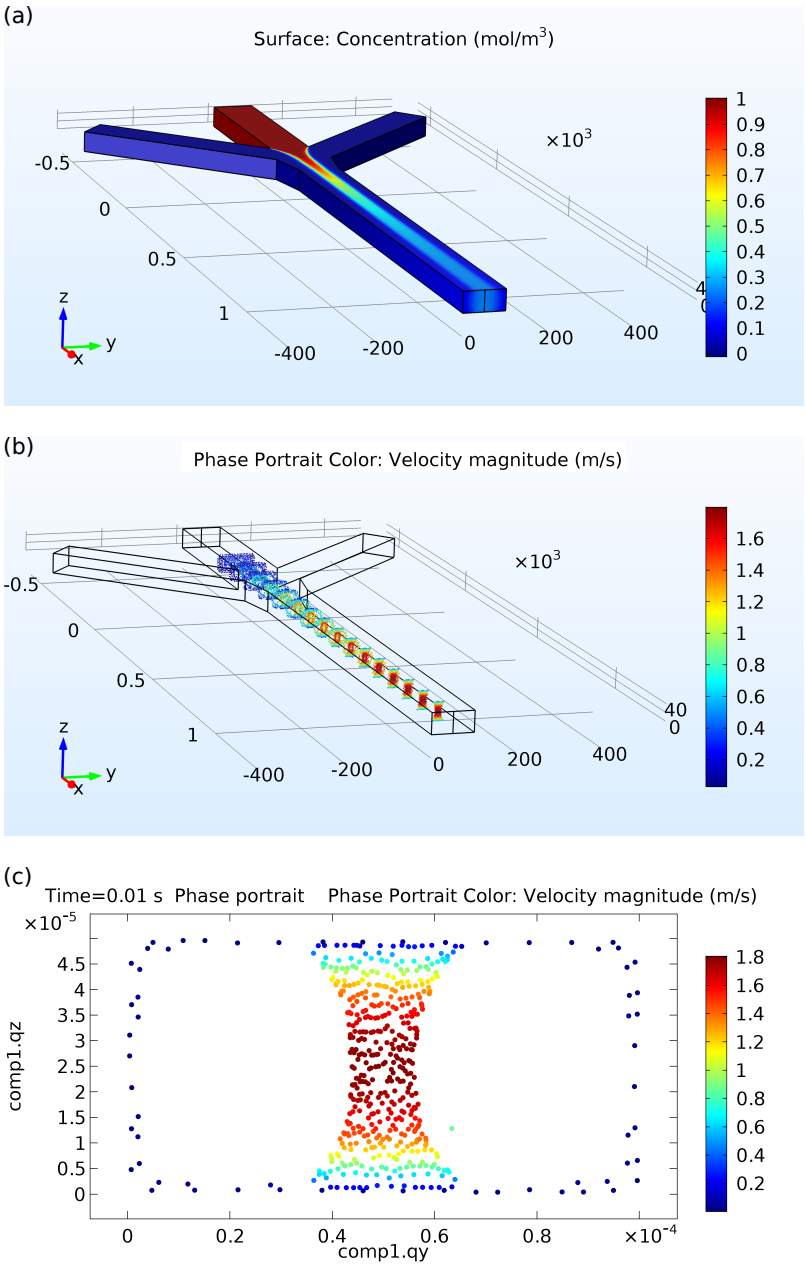

Figure 6.6: Comsol simulations of a 100 µm wide by 50 µm microfluidic channel junction designed to focus cells (introduced in the center channel) into the center of the channel using a sheath fluid introduced in the angled inlets. Shown are (a) transport of diluted species (colormap represents dilution) and (b-c) particle tracing results (colormap represents particle velocity).

Chapter 7

Conclusion

This thesis has presented several techniques for high-speed signal acquisition using optical processing of ultrafast pulses. Efficient real-time analog compression of sparse-frequency RF waveforms as well as complex optical images was implemented, significantly reducing the required number of measurements to $\sim 1\%$ of Nyquist and lower. Several new approaches to high-speed quantitative phase microscopy were introduced, which improve the efficiency and robustness of interferometric time-stretch microscopy. By altering the CS measurement matrix, it should be possible to marry the compression and quantitative phase information in future work.

Bibliography

[1] L. Rayleigh, "On the passage of electric waves through tubes, or the vibrations of dielectric cylinders," *The London, Edinburgh, and Dublin Philosophical Magazine and Journal of Science*, vol. 43, no. 261, pp. 125–132, 1897.

[2] J. J. Thomson, *Notes on Recent Researches in Electricity and Magnetism*. Clarendon Press, 1893.

[3] G. C. Southworth, "Survey and History of the Progress of the Microwave Arts," *Proceedings of the IRE*, vol. 50, no. 5, pp. 1199–1206, may 1962.

[4] G. P. Agrawal, *Fiber-Optic Communication Systems*. John Wiley & Sons, 2012.

[5] ——, *Nonlinear fiber optics*. Academic press, 2007.

[6] R. Pleban, A. Azari, R. Salem, and T. E. Murphy, "SSPROP," 2006.

[7] A. Weiner, *Ultrafast Optics*. John Wiley & Sons, 2009.

[8] E. L. Wooten, K. M. Kissa, A. Yi-Yan, E. J. Murphy, D. A. Lafaw, P. F. Hallemeier, D. Maack, D. V. Attanasio, D. J. Fritz, G. J. McBrien, and Others, "A review of lithium niobate modulators for fiber-optic communications systems," *IEEE Journal of Selected Topics in Quantum Electronics*, vol. 6, no. 1, pp. 69–82, 2000.

[9] E. Desurvire, J. R. Simpson, and P. C. Becker, "High-gain erbium-doped traveling-wave fiber amplifier," *Optics Letters*, vol. 12, no. 11, p. 888, 1987.

[10] M. E. Fermann, V. da Silva, D. A. Smith, Y. Silberberg, and A. M. Weiner, "Shaping of ultrashort optical pulses by using an integrated acousto-optic tunable filter," *Optics Letters*, vol. 18, no. 18, pp. 1505–1507, 1993.

[11] P. Tournois, "Acousto-optic programmable dispersive filter for adaptive compensation of group delay time dispersion in laser systems," *Optics Communications*, vol. 140, no. 4, pp. 245–249, 1997.

[12] A. Weiner, "Femtosecond optical pulse shaping and processing," *Progress in Quantum Electronics*, vol. 19, no. 3, pp. 161–237, 1995.

[13] D. E. Leaird and A. M. Weiner, "Femtosecond optical packet generation by a direct space-to-time pulse shaper," *Optics Letters*, vol. 24, no. 12, pp. 853–855, 1999.

BIBLIOGRAPHY

[14] I. S. Lin, J. D. McKinney, and A. M. Weiner, "Photonic synthesis of broadband microwave arbitrary waveforms applicable to ultra-wideband communication," *IEEE Microwave and Wireless Components Letters*, vol. 15, no. 4, pp. 226–228, 2005.

[15] F. Verluise, V. Laude, Z. Cheng, C. Spielmann, and P. Tournois, "Amplitude and phase control of ultrashort pulses by use of an acousto-optic programmable dispersive filter: pulse compression and shaping," *Optics Letters*, vol. 25, no. 8, pp. 575–577, 2000.

[16] J. W. Goodman, *Introduction to Fourier Optics*. Roberts and Company Publishers, 2005.

[17] O. E. Martinez, J. P. Gordon, and R. L. Fork, "Negative group-velocity dispersion using refraction," *Journal of the Optical Society of America A*, vol. 1, no. 10, p. 1003, 1984.

[18] O. E. Martinez, "3000 times grating compressor with positive group velocity dispersion: Application to fiber compensation in 1.3-1.6 μm region," *IEEE Journal of Quantum Electronics*, vol. 23, no. 1, pp. 59–64, 1987.

[19] P. Maine, D. Strickland, P. Bado, M. Pessot, and G. Mourou, "Generation of ultrahigh peak power pulses by chirped pulse amplification," *IEEE Journal of Quantum Electronics*, vol. 24, no. 2, pp. 398–403, 1988.

BIBLIOGRAPHY

[20] B. H. Kolner, "Space-Time Duality and the Theory of Temporal Imaging," *IEEE Journal of Quantum Electronics*, vol. 30, no. 8, pp. 1951–1963, aug 1994.

[21] A. Papoulis, "Pulse compression, fiber communications, and diffraction: a unified approach," *Journal of the Optical Society of America A*, vol. 11, no. 1, p. 3, jan 1994.

[22] E. Candès and T. Tao, "Near-Optimal Signal Recovery From Random Projections: Universal Encoding Strategies?" *IEEE Transactions on Information Theory*, vol. 52, no. 12, pp. 5406–5425, 2006.

[23] E. J. Candès, J. Romberg, and T. Tao, "Robust Uncertainty Principles : Exact Signal Frequency Information," *IEEE Transactions on Information Theory*, vol. 52, no. 2, pp. 489–509, 2006.

[24] E. J. Candès, J. K. Romberg, and T. Tao, "Stable signal recovery from incomplete and inaccurate measurements," *Communications on Pure and Applied Mathematics*, vol. 59, no. 8, pp. 1207–1223, 2006.

[25] E. J. Candès and T. Tao, "Decoding by linear programming," *IEEE Transactions on Information Theory*, vol. 51, no. 12, pp. 4203–4215, 2005.

[26] D. L. Donoho, "Compressed sensing," *IEEE Transactions on Information Theory*, vol. 52, no. 4, pp. 1289–1306, 2006.

BIBLIOGRAPHY

[27] J. Zhang, Y. Suo, S. Mitra, S. P. Chin, S. Hsiao, R. F. Yazicioglu, T. D. Tran, and R. Etienne-Cummings, "An efficient and compact compressed sensing microsystem for implantable neural recordings," *IEEE Transactions on Biomedical Circuits and Systems*, vol. 8, no. 4, pp. 485–496, 2014.

[28] J. Zhang, T. Xiong, T. Tran, S. Chin, and R. Etienne-Cummings, "Compact all-CMOS spatiotemporal compressive sensing video camera with pixel-wise coded exposure," *Optics Express*, vol. 24, no. 8, pp. 9013–9024, 2016.

[29] L. Gao, J. Liang, C. Li, and L. V. Wang, "Single-shot compressed ultrafast photography at one hundred billion frames per second," *Nature*, vol. 516, no. 7529, pp. 74–77, 2014.

[30] E. J. Candès and M. B. Wakin, "An introduction to compressive sampling," *IEEE Signal Processing Magazine*, vol. 25, no. 2, pp. 21–30, 2008.

[31] D. Takhar, J. N. Laska, M. B. Wakin, M. F. Duarte, D. Baron, S. Sarvotham, K. F. Kelly, and R. G. Baraniuk, "A new compressive imaging camera architecture using optical-domain compression," *Proc. SPIE*, vol. 6065, pp. 606 509–606 510, 2006.

[32] M. F. Duarte, M. A. Davenport, D. Takhar, J. N. Laska, T. Sun, K. F. Kelly, and R. G. Baraniuk, "Single-Pixel Imaging via Compressive Sampling," *IEEE Signal Processing Magazine*, vol. 25, no. 2, pp. 83–91, mar 2008.

BIBLIOGRAPHY

[33] A. Bleicher, "Peaceful coexistence," *IEEE Spectrum*, vol. 50, no. 4, pp. 42–56, 2013.

[34] J. M. Nichols and F. Bucholtz, "Beating Nyquist with light: a compressively sampled photonic link," *Optics Express*, vol. 19, no. 8, p. 7339, apr 2011.

[35] J. A. Tropp, J. N. Laska, M. F. Duarte, J. K. Romberg, and R. G. Baraniuk, "Beyond Nyquist: Efficient sampling of sparse bandlimited signals," *IEEE Transactions on Information Theory*, vol. 56, no. 1, pp. 520–544, 2010.

[36] L. Yan, Y. Dai, K. Xu, J. Wu, Y. Li, Y. Ji, and J. Lin, "Integrated multifrequency recognition and downconversion based on photonics-assisted compressive sampling," *IEEE Photonics Journal*, vol. 4, no. 3, pp. 664–670, 2012.

[37] G. C. Valley, G. A. Sefler, and T. J. Shaw, "Compressive sensing of sparse radio frequency signals using optical mixing," *Optics Letters*, vol. 37, no. 22, p. 4675, 2012.

[38] H. Nan, Y. Gu, and H. Zhang, "Optical analog-to-digital conversion system based on compressive sampling," *IEEE Photonics Technology Letters*, vol. 23, no. 2, pp. 67–69, 2011.

[39] H. Chi, Y. Mei, Y. Chen, D. Wang, S. Zheng, X. Jin, and X. Zhang, "Microwave spectral analysis based on photonic compressive sampling with random demodulation," *Optics Letters*, vol. 37, no. 22, p. 4636, 2012.

BIBLIOGRAPHY

[40] H. Chi, Y. Chen, Y. Mei, X. Jin, S. Zheng, and X. Zhang, "Microwave spectrum sensing based on photonic time stretch and compressive sampling," *Optics Letters*, vol. 38, no. 2, p. 136, 2013.

[41] F. Coppinger, A. S. Bhushan, and B. Jalali, "Photonic time stretch and its application to analog-to-digital conversion," *IEEE Transactions on Microwave Theory and Techniques*, vol. 47, no. 7 PART 2, pp. 1309–1314, 1999.

[42] M. A. Figueiredo, R. D. Nowak, and S. J. Wright, "Gradient projection for sparse reconstruction: Application to compressed sensing and other inverse problems," *IEEE Journal on Selected Topics in Signal Processing*, vol. 1, no. 4, pp. 586–597, 2007.

[43] D. Cabric, S. Mishra, and R. Brodersen, "Implementation issues in spectrum sensing for cognitive radios," in *Asilomar Conference on Signals, Systems and Computers*. IEEE, 2004, vol. 1, pp. 772–776.

[44] H. Sun, A. Nallanathan, C.-X. Wang, and Y. Chen, "Wideband spectrum sensing for cognitive radio networks: A survey," *IEEE Wireless Communications*, vol. 20, no. 2, pp. 74–81, apr 2013.

[45] Y. Liang, M. Chen, H. Chen, C. Lei, P. Li, and S. Xie, "Photonic-assisted multichannel compressive sampling based on effective time delay pattern," *Optics Express*, vol. 21, no. 22, p. 25700, nov 2013.

BIBLIOGRAPHY

[46] Y. Chen, X. Yu, H. Chi, S. Zheng, X. Zhang, X. Jin, and M. Galili, "Compressive sensing with a microwave photonic fi lter," *Optics Communications*, vol. 338, pp. 428–432, 2015.

[47] C. Wang, M. Li, and J. Yao, "Continuously tunable photonic microwave frequency multiplication by use of an unbalanced temporal pulse shaping system," *IEEE Photonics Technology Letters*, vol. 22, no. 17, pp. 1285–1287, sep 2010.

[48] M. Li and J. Yao, "All-optical short-time Fourier transform based on a temporal pulse-shaping system incorporating an array of cascaded linearly chirped fiber Bragg gratings," *IEEE Photonics Technology Letters*, vol. 23, no. 20, pp. 1439–1441, 2011.

[49] ——, "Ultrafast all-optical Wavelet transform based on temporal pulse shaping incorporating a 2-D array of cascaded linearly chirped fiber bragg gratings," *IEEE Photonics Technology Letters*, vol. 24, no. 15, pp. 1319–1321, aug 2012.

[50] B. T. Bosworth and M. A. Foster, "High-speed ultrawideband photonically enabled compressed sensing of sparse radio frequency signals," *Optics Letters*, vol. 38, no. 22, pp. 4892–4895, 2013.

[51] M. Mishali, Y. C. Eldar, and A. J. Elron, "Xampling: Signal acquisition and processing in union of subspaces," *IEEE Transactions on Signal Processing*, vol. 59, no. 10, pp. 4719–4734, oct 2011.

BIBLIOGRAPHY

[52] Y. Chi, L. L. Scharf, A. Pezeshki, and A. R. Calderbank, "Sensitivity to basis mismatch in compressed sensing," *IEEE Transactions on Signal Processing*, vol. 59, no. 5, pp. 2182–2195, may 2011.

[53] M. F. Duarte and R. G. Baraniuk, "Spectral compressive sensing toolbox," *Applied and Computational Harmonic Analysis*, vol. 35, pp. 111–129, 2013.

[54] C. V. McLaughlin, J. M. Nichols, and F. Bucholtz, "Basis mismatch in a compressively sampled photonic link," *IEEE Photonics Technology Letters*, vol. 25, no. 23, pp. 2297–2300, 2013.

[55] G. C. Valley and T. J. Shaw, "Applications of the Orthogonal Matching Pursuit / Nonlinear Least Squares Algorithm to Compressive Sensing Recovery," in *Applications of Digital Signal Processing*, C. Cuadrado-Laborde, Ed. Intech, 2011, pp. 169–190.

[56] G. C. Valley, G. A. Sefler, and T. J. Shaw, "Sensing RF signals with the optical wideband converter," *Proc. SPIE*, vol. 8645, pp. 1–10, 2013.

[57] J. M. Nichols, A. K. Oh, and R. M. Willett, "Reducing basis mismatch in harmonic signal recovery via alternating convex search," *IEEE Signal Processing Letters*, vol. 21, no. 8, pp. 1007–1011, aug 2014.

BIBLIOGRAPHY

[58] J. M. Nichols, F. Bucholtz, C. V. McLaughlin, A. K. Oh, and R. M. Willett, "Fixing basis mismatch in compressively sampled photonic link," *Proc. SPIE*, vol. 9118, p. 91180N, 2014.

[59] T. P. McKenna, M. D. Sharp, D. G. Lucarelli, J. A. Nanzer, M. L. Dennis, and T. R. Clark, "Wideband Photonic Compressive Sampling Analog-to-Digital Converter for RF Spectrum Estimation," in *Optical Fiber Communication Conference/National Fiber Optic Engineers Conference 2013*. Optical Society of America, 2013, p. OTh3D.1.

[60] S. Smaili and Y. Massoud, "Accurate and efficient modeling of random demodulation based compressive sensing systems with a general filter," in *IEEE International Symposium on Circuits and Systems*. IEEE, jun 2014, pp. 2519–2522.

[61] J. R. Stroud, B. T. Bosworth, D. Tran, T. McKenna, T. Clark, T. Tran, S. Chin, and M. A. Foster, "Continuous 119.2-GSample/s Photonic Compressed Sensing of Sparse Microwave Signals," in *Conference on Lasers and Electro-Optics (CLEO)*. Optical Society of America, 2015.

[62] J. A. Tropp, "Algorithms for simultaneous sparse approximation.Part I and Part II," *Signal Processing*, vol. 86, no. 3, pp. 589–602, 2006.

[63] H. M. Shapiro, *Practical Flow Cytometry*, 4th ed. Hoboken, N.J.: Wiley, 2003.

BIBLIOGRAPHY

[64] M. Leach, M. Drummond, and A. Doig, *contents, Practical Flow Cytometry in Haematology Diagnosis*. Hoboken, N.J.: Wiley, 2013.

[65] G. Grégori, B. Rajwa, V. Patsekin, J. Jones, M. Furuki, M. Yamamoto, and J. Paul Robinson, "Hyperspectral cytometry," in *Current Topics in Microbiology and Immunology*, H. G. Fienberg and G. P. Nolan, Eds. Heidelberg: Springer, 2013, vol. 377, pp. 191–210.

[66] J. F. Leary, "Rare-Event Detection and Sorting of Rare Cells," in *Emerging Tools for Single-Cell Analysis: Advances in Optical Measurement Technologies*, G. Durack and J. P. Robinson, Eds. New York: Wiley, 2000, vol. 3, pp. 49–72.

[67] A. Krishan, H. Krishnamurthy, and S. Totey, *Applications of Flow Cytometry in Stem Cell Research and Tissue Regeneration*. Hoboken, N.J.: Wiley, 2011.

[68] L. E. Lowes, D. Goodale, M. Keeney, and A. L. Allan, "Image cytometry analysis of circulating tumor cells," in *Methods in Cell Biology*, 5th ed., Z. Darzynkiewicz, E. Holden, A. Orfao, W. Telford, and D. Wlodkowic, Eds. San Diego: Elsevier Science, 2011, vol. 102, pp. 261–290.

[69] D. a. Basiji, W. E. Ortyn, L. Liang, V. Venkatachalam, and P. Morrissey, "Cellular image analysis and imaging by flow cytometry," *Clinics in Laboratory Medicine*, vol. 27, no. 3, pp. 653–670, 2007.

BIBLIOGRAPHY

[70] E. K. Zuba-Surma and M. Z. Ratajczak, "Analytical capabilities of the imagestream cytometer," in *Methods in Cell Biology*, 5th ed., Z. Darzynkiewicz, E. Holden, A. Orfao, W. Telford, and D. Wlodkowic, Eds. San Diego: Elsevier Science, 2011, vol. 102, pp. 207–230.

[71] "INSPIRE ImageStream^X System Software User's Manual," 2010.

[72] D. J. Ehrlich, B. K. McKenna, J. G. Evans, A. C. Belkina, G. V. Denis, D. H. Sherr, and M. C. Cheung, "Parallel imaging microfluidic cytometer," in *Methods in Cell Biology*, 5th ed., Z. Darzynkiewicz, E. Holden, A. Orfao, W. Telford, and D. Wlodkowic, Eds. San Diego: Elsevier Science, 2011, vol. 102, pp. 49–75.

[73] H. R. Petty, "Spatiotemporal chemical dynamics in living cells: From information trafficking to cell physiology," *BioSystems*, vol. 83, no. 2-3, pp. 217–224, 2006.

[74] P. Lang, K. Yeow, A. Nichols, and A. Scheer, "Cellular imaging in drug discovery." *Nature Reviews Drug Discovery*, vol. 5, no. 4, pp. 343–356, 2006.

[75] E. Brouzes, M. Medkova, N. Savenelli, D. Marran, M. Twardowski, J. B. Hutchison, J. M. Rothberg, D. R. Link, N. Perrimon, and M. L. Samuels, "Droplet microfluidic technology for single-cell high-throughput screening," *Proceedings of the National Academy of Sciences*, vol. 106, no. 34, pp. 14 195–14 200, 2009.

BIBLIOGRAPHY

[76] K. Goda, a. Ayazi, D. R. Gossett, J. Sadasivam, C. K. Lonappan, E. Sollier, a. M. Fard, S. C. Hur, J. Adam, C. Murray, C. Wang, N. Brackbill, D. Di Carlo, and B. Jalali, "High-throughput single-microparticle imaging flow analyzer," *Proceedings of the National Academy of Sciences*, vol. 109, no. 29, pp. 11 630–11 635, 2012.

[77] N. Rimon and M. Schuldiner, "Getting the whole picture: combining throughput with content in microscopy," *Journal of Cell Science*, vol. 124, no. 22, pp. 3743–3751, 2011.

[78] W. M. Weaver, P. Tseng, A. Kunze, M. Masaeli, A. J. Chung, J. S. Dudani, H. Kittur, R. P. Kulkarni, and D. Di Carlo, "Advances in high-throughput single-cell microtechnologies," *Current Opinion in Biotechnology*, vol. 25, no. 0, pp. 114–123, 2014.

[79] K. Goda, K. K. Tsia, and B. Jalali, "Serial time-encoded amplified imaging for real-time observation of fast dynamic phenomena," *Nature*, vol. 458, no. 7242, pp. 1145–1149, 2009.

[80] T. T. W. Wong, A. K. S. Lau, K. K. Y. Wong, and K. K. Tsia, "Optical time-stretch confocal microscopy at 1 μm," *Optics Letters*, vol. 37, no. 16, pp. 3330–3332, aug 2012.

BIBLIOGRAPHY

[81] A. Mahjoubfar, C. Chen, K. R. Niazi, S. Rabizadeh, and B. Jalali, "Label-free high-throughput cell screening in flow." *Biomedical Optics Express*, vol. 4, no. 9, pp. 1618–25, 2013.

[82] T. T. W. Wong, A. K. S. Lau, K. K. Y. Ho, M. Y. H. Tang, J. D. F. Robles, X. Wei, A. C. S. Chan, A. H. L. Tang, E. Y. Lam, K. K. Y. Wong, G. C. F. Chan, H. C. Shum, and K. K. Tsia, "Asymmetric-detection time-stretch optical microscopy (ATOM) for ultrafast high-contrast cellular imaging in flow." *Scientific Reports*, vol. 4, p. 3656, 2014.

[83] F. Xing, H. Chen, C. Lei, Z. Weng, M. Chen, S. Yang, and S. Xie, "Serial wavelength division 1GHz line-scan microscopic imaging," *Photonics Research*, vol. 2, no. 4, p. B31, aug 2014.

[84] H. Chen, C. Lei, F. Xing, Z. Weng, M. Chen, S. Yang, and S. Xie, "Multiwavelength time-stretch imaging system," *Optics Letters*, vol. 39, no. 7, p. 2202, 2014.

[85] M. El-desouki, M. J. Deen, Q. Fang, L. Liu, F. Tse, and D. Armstrong, "CMOS Image Sensors for High Speed Applications," *Sensors*, vol. 9, no. 1, pp. 430–444, 2009.

[86] T. G. Etoh, D. V. T. Son, T. Yamada, and E. Charbon, "Toward One Giga Frames per Second—Evolution of in Situ Storage Image Sensors," *Sensors*, vol. 13, no. 4, pp. 4640–4658, 2013.

BIBLIOGRAPHY

[87] T. Arai, J. Yonai, T. Hayashida, H. Ohtake, H. van Kuijk, and T. G. Etoh, "Back-side-illuminated image sensor with burst capturing speed of 5.2 Tpixel per second," *Proc. SPIE*, vol. 8659, pp. 865 904–865 904–10, 2013.

[88] K. Nakagawa, A. Iwasaki, Y. Oishi, R. Horisaki, A. Tsukamoto, A. Nakamura, K. Hirosawa, H. Liao, T. Ushida, K. Goda, F. Kannari, and I. Sakuma, "Sequentially timed all-optical mapping photography (STAMP)," *Nature Photonics*, vol. 8, no. 9, pp. 695–700, 2014.

[89] C. Azeredo-Leme, "Clock Jitter Effects on sampling: A tutorial," *IEEE Circuits and Systems Magazine*, vol. 11, no. 3, pp. 26–37, 2011.

[90] R. G. Baraniuk, "Compressive sensing," *IEEE Signal Processing Magazine*, vol. 24, no. 4, pp. 118–124, 2007.

[91] Y. Chen, X. Yu, H. Chi, X. Jin, X. Zhang, S. Zheng, and M. Galili, "Compressive sensing in a photonic link with optical integration," *Optics Letters*, vol. 39, no. 8, p. 2222, 2014.

[92] M. H. Asghari and B. Jalali, "Anamorphic transformation and its application to time-bandwidth compression," *Applied Optics*, vol. 52, no. 27, pp. 6735–6743, 2013.

[93] ——, "Experimental demonstration of optical real-time data compressiona," *Applied Physics Letters*, vol. 104, no. 11, p. 111101, 2014.

BIBLIOGRAPHY

[94] B. T. Bosworth and M. A. Foster, "High-speed flow imaging utilizing spectral-encoding of ultrafast pulses and compressed sensing," in *Conference on Lasers and Electro-Optics (CLEO)*, no. Mll. Optical Society of America, 2014, p. ATh4P.3.

[95] A. Chan, A. Lau, and K. Wong, "Two-dimensional spectral-encoding for high speed arbitrary patterned illumination," in *Conference on Lasers and Electro-Optics (CLEO)*, no. 1. Optical Society of America, 2014, pp. 1–2.

[96] H. Chen, Z. Weng, Y. Liang, C. Lei, F. Xing, M. Chen, and S. Xie, "High speed single-pixel imaging via time domain compressive sampling," in *Conference on Lasers and Electro-Optics (CLEO)*. Optical Society of America, 2014, p. JTh2A.132.

[97] A. C. S. Chan, E. Y. Lam, and K. K. Tsia, "Signal reduction in fluorescence imaging using radio frequency-multiplexed excitation by compressed sensing," *Proc. SPIE*, vol. 9279, p. 92790U, 2014.

[98] D. S. Taubman, M. W. Marcellin, and M. Rabbani, *JPEG2000: Image Compression Fundamentals, Standards and Practice*. Springer, 2002, vol. 11, no. 2.

[99] S. Mallat, *A Wavelet Tour of Signal Processing: The Sparse Way*. Academic, 2008.

[100] F. Magalhães, F. M. Araújo, M. V. Correia, M. Abolbashari, and F. Farahi, "Active illumination single-pixel camera based on compressive sensing." *Applied Optics*, vol. 50, no. 4, pp. 405–414, 2011.

[101] V. Studer, J. Bobin, M. Chahid, H. S. Mousavi, E. Candes, and M. Dahan, "Compressive fluorescence microscopy for biological and hyperspectral imaging," *Proceedings of the National Academy of Sciences*, vol. 109, no. 26, pp. E1679–E1687, 2012.

[102] B. C. Grubel, B. T. Bosworth, M. R. Kossey, H. Sun, A. B. Cooper, M. A. Foster, and A. C. Foster, "Silicon photonic physical unclonable function," *Optics Express*, vol. 25, no. 11, p. 12710, may 2017.

[103] S. A. Diddams, L. Hollberg, and V. Mbele, "Molecular fingerprinting with the resolved modes of a femtosecond laser frequency comb," *Nature*, vol. 445, no. 7128, pp. 627–630, 2007.

[104] J. Yang, X. Yuan, X. Liao, P. Llull, D. J. Brady, G. Sapiro, and L. Carin, "Video compressive sensing using gaussian mixture models," *IEEE Transactions on Image Processing*, vol. 23, no. 11, pp. 4863–4878, nov 2014.

[105] D. R. Solli, J. Chou, and B. Jalali, "Amplified wavelengthtime transformation for real-time spectroscopy," *Nature Photonics*, vol. 2, no. 1, pp. 48–51, 2008.

[106] J. XU, C. Zhang, J. Xu, K. K. Y. Wong, and K. K. Tsia, "5 MHz all-optical swept-source optical coherence tomography based on amplified dispersive Fourier transform," in *Optics in the Life Sciences*. Optical Society of America, 2013, p. NW5B.5.

[107] T. Jannson, "Real-time Fourier transformation in dispersive optical fibers," *Optics Letters*, vol. 8, no. 4, p. 232, 1983.

[108] F. Xing, H. Chen, M. Chen, S. Yang, and S. Xie, "Simple approach for fast real-time line scan microscopic imaging." *Applied Optics*, vol. 52, no. 28, pp. 7049–7053, 2013.

[109] A. M. Fard, A. Mahjoubfar, K. Goda, D. R. Gossett, D. Di Carlo, and B. Jalali, "Nomarski serial time-encoded amplified microscopy for high-speed contrast-enhanced imaging of transparent media." *Biomedical Optics Express*, vol. 2, no. 12, pp. 3387–92, 2011.

[110] A. K. S. Lau, T. T. W. Wong, K. K. Y. Ho, M. T. H. Tang, A. C. S. Chan, X. Wei, E. Y. Lam, H. C. Shum, K. K. Y. Wong, and K. K. Tsia, "Interferometric time-stretch microscopy for ultrafast quantitative cellular and tissue imaging at 1 μm," *Journal of Biomedical Optics*, vol. 19, no. 7, p. 076001, 2014.

[111] C. L. Chen, A. Mahjoubfar, L.-C. Tai, I. K. Blaby, A. Huang, K. R. Niazi, and B. Jalali, "Deep Learning in Label-free Cell Classification," *Scientific Reports*, vol. 6, no. 1, p. 21471, 2016.

[112] F. Xing, H. Chen, S. Xie, and S. Member, "Ultrafast Three-Dimensional Surface Imaging Based on Short-Time Fourier Transform," vol. 27, no. 21, pp. 2264–2267, 2015.

[113] D. K. Hamilton, C. J. R. Sheppard, and J. R. Sheppard, "Differential phase contrast in scanning optical microscopy," *Journal of Microscopy*, vol. 133, pp. 27–39, 1984.

[114] A. K. S. Lau, A. H. L. Tang, K. K. Y. Wong, and K. K. Tsia, "Quantitative phase asymmetric-detection time-stretch optical microscopy (Q-ATOM) for ultrafast cellular imaging," in *Biomedical Optics*, vol. 28. Optical Society of America, 2014, pp. 35–37.

[115] C. Dorrer and I. Kang, "Highly sensitive direct characterization of femtosecond pulses by electro-optic spectral shearing interferometry," *Optics Letters*, vol. 28, no. 6, p. 477, 2003.

[116] C. Dorrer and J. Bromage, "High-sensitivity optical pulse characterization using Sagnac electro-optic spectral shearing interferometry." *Optics Letters*, vol. 35, no. 9, pp. 1353–5, 2010.

[117] B. T. Bosworth and M. A. Foster, "High-speed spectral shearing contrast time-stretch microscopy," in *Conference on Lasers and Electro-Optics (CLEO)*, 2016, p. SM1O.3.

[118] D. Di Carlo, D. Irimia, R. G. Tompkins, and M. Toner, "Continuous inertial focusing, ordering, and separation of particles in microchannels." *Proceedings of the National Academy of Sciences*, vol. 104, no. 48, pp. 18 892–18 897, 2007.

[119] J. M. K. Ng, I. Gitlin, A. D. Stroock, and G. M. Whitesides, "Components for integrated poly(dimethylsiloxane) microfluidic systems," *Electrophoresis*, vol. 23, no. 20, pp. 3461–3473, 2002.

[120] N. Delen and B. Hooker, "Free-space beam propagation between arbitrarily oriented planes based on full diffraction theory: a fast Fourier transform approach," *Journal of the Optical Society of America A*, vol. 15, no. 4, p. 857, 1998.

[121] N. D. Mehendale and D. Paul, "Hydrodynamic Flow Focusing for Microfluidic Cell Sorting Chip," in *COMSOL Conference*, 2014.

[122] D. R. Gossett, H. T. K. Tse, S. A. Lee, Y. Ying, A. G. Lindgren, O. O. Yang, J. Rao, A. T. Clark, and D. Di Carlo, "Hydrodynamic stretching of single cells for large population mechanical phenotyping," *Proceedings of the National Academy of Sciences*, vol. 109, no. 20, pp. 7630–7635, 2012.

[123] O. Otto, P. Rosendahl, A. Mietke, S. Golfier, C. Herold, D. Klaue, S. Girardo, S. Pagliara, A. Ekpenyong, A. Jacobi, M. Wobus, N. Topfner, U. F. Keyser, J. Mansfeld, E. Fischer-Friedrich, and J. Guck, "Real-time deformability cytom-

etry: on-the-fly cell mechanical phenotyping," *Nature Methods*, vol. 12, no. 3, pp. 199–202, 2015.

[124] M. Xavier, P. Rosendahl, M. Herbig, M. Kräter, D. Spencer, M. Bornhäuser, R. O. C. Oreffo, H. Morgan, J. Guck, and O. Otto, "Mechanical phenotyping of primary human skeletal stem cells in heterogeneous populations by real-time deformability cytometry," *Integrative Biology*, vol. 8, no. 5, pp. 616–623, 2016.

Vita

Bryan T. Bosworth completed his B.S. in Electrical Engineering at Princeton University. Before coming to Johns Hopkins, he was a Fulbright scholar at the Albert-Ludwigs-Universität Freiburg and a DAAD RISE Professional student at SMA Solar Technology AG in Niestetal, Germany.